Physics – Uspekhi **65** (1) 62 – 89 (2022)

REVIEWS OF TOPICAL PROBLEMS PACS numbers: 47.27.er, **95.75.–z**

Wavelets for the space-time structure analysis of physical fields

P G Frick, D D Sokoloff, R A Stepanov

DOI: https://doi.org/10.3367/UFNe.2020.10.038859

Contents

Abstract. Spectral analysis, based on the Fourier method, is a general tool in physics. Wavelets appeared as a natural generalization of classical spectral analysis to the case of complex nonstationary and spatially inhomogeneous systems, for which a comparison with an infinite sinusoid, which forms the basis of the Fourier method, has to be replaced by a comparison with a finite wave packet, which is known as a wavelet. In this review, the authors, based largely on their own experience of application wavelet analysis in astro- and geophysics, solar-terrestrial relations, as well as climatology, medical physics, and laboratory hydrodynamic experiments, demonstrate the possibilities and discuss the practical aspects of the application of the wavelet apparatus to the interpretation of signals and images of various physical natures.

P G Frick [1,2,a], **D D Sokoloff** [3,4,5,b], **R A Stepanov** [1,6,c]
[1] Institute of Continuous Media Mechanics,
Ural Branch of the Russian Academy of Sciences,
ul. Akademika Koroleva 1, 614013 Perm, Russian Federation
[2] Perm State National Research University,
ul. Bukireva 15, 614068 Perm, Russian Federation
[3] Lomonosov Moscow State University, Department of Physics,
Leninskie gory 1, 119991 Moscow, Russian Federation
[4] Moscow Center for Fundamental and Applied Mathematics,
Leninskie gory 1, 119991 Moscow, Russian Federation
[5] Pushkov Institute of Terrestrial Magnetism,
Ionosphere and Radio Wave Propagation,
Russian Academy of Sciences,
Kaluzhskoe shosse 4, 108840 Troitsk, Moscow, Russian Federation
[6] Perm National Research Polytechnic University,
prosp. Komsomol'skii 29, 614990 Perm, Russian Federation
E-mail: [a] frick@icmm.ru, [b] sokoloff.dd@gmail.com,
[c] rodion@icmm.ru

Received 8 August 2020, revised 20 October 2020
Uspekhi Fizicheskikh Nauk **192** (1) 69 – 99 (2022)
Translated by Yu V Morozov

Keywords: wavelets, spectral analysis, data processing for signals and images, solar and stellar activity, galactic magnetic fields, geophysics, medical physics

1. Introduction

The decomposition of a signal based on harmonic functions is rightly considered a natural means for the study of periodic components of various signals. The idea of this analysis is mathematically formalized, in particular, in the form of the Fourier transform

$$\hat{f}(\omega) = \int_{-\infty}^{+\infty} f(t) \exp(\mathrm{i}\omega t)\, \mathrm{d}t\,. \qquad (1)$$

The complex function $\hat{f}(\omega)$ represents the spectral composition of an analyzed signal $f(t)$ showing the amplitude and the phase of the contribution that an oscillation with circular frequency ω makes to it. Integral (1) must be convergent, i.e., the function $f(t)$ is assumed, in a sense, to decrease at infinity. However, this seemingly natural requirement does not always correspond to the physical content of the problem. For example, let $f(t)$ be a signal transmitted by some radio station (more specifically, the value at a given point of one of the components of the electric vector of the generated electromagnetic field). Such signal is localized in time: it was obviously absent before the development of radio communication, and the radio station transmitting it will certainly cease to exist with time or will change the operating frequency. However, this general consideration hardly helps to calculate integral (1). In fact, we are interested not so much in the nominal frequency of the radio station signal that is usually known as in the changes in the spectral composition of this signal over time that actually carry the information transmitted by the radio station. Expression (1) does not by itself have the means to detect these modulations.

Strictly speaking, the Fourier analysis is applicable to time-*limited* signals. Then, if a signal does not contain nonintegrable singularities, there is integral (1), called the continuous Fourier transform. It is also used for periodic signals, such that $f(t+T)=f(t)$, for which expansion in a Fourier series that is a discrete form of the Fourier transform is possible. Finally, the analysis can be applied to *statistically stationary* signals, the autocorrelation function of which decays and, according to the Wiener–Khinchin theorem [1] (see, for example, [1]), allows the power spectral density (PSD) of the signal to be calculated.

Obviously, a possible approach to the problem of analyzing signals, the spectral composition of which changes with time, is to calculate the Fourier transform locally, i.e., in the vicinity of a given moment of time t' while disregarding a signal at a considerable time distance from the moment of interest. This is exactly what different variants of the Windowed Fourier transform do (it is also known as the Gabor transform [2], where t' is an additional independent variable). For a radio signal, this algorithm is easy to implement, since the signal carrier frequency that ensures transmission is much higher than the frequencies carrying the transmitted meaningful information; true, in this case, it is worth considering whether the way in which a part of the signal is cut out creates any artifacts. However, physical systems under natural conditions as a rule do not display a pronounced division of characteristic time scales. Nonlinearity leads to both fast modulation (amplitude or phase) of the fundamental natural frequency (if any) and a noticeable change in the shape of oscillations. For example, the pulse of a healthy person at rest is relatively stable and rather smoothly modulated by breathing. The picture changes markedly as soon as one begins to physically exert oneself. Another example is the magnetic activity of the Sun undergoing famous 11-year cycles reliably reconstructed from data collected for centuries of numerous observations. However, it is important to know not only the average parameters of a cycle but also their dynamics (which becomes clear during 2–3 consecutive oscillations) if a relevant physical theory is to be developed.

A fundamental step is to abandon the standard with an infinite number of periods and introduce a new wave standard with a limited number of cycles (hereinafter referred to as a wavelet) which is a quasiperiodic function in the strict sense. This can be done, for example, by multiplying the harmonic function by the Gaussian envelope $\exp(2\pi i t - t^2/\sigma^2)$, where the parameter σ is responsible for the effective number of cycles. Using translation and dilatation/compression transformations, we obtain the basis of functions for the decomposition of $f(t)$. Thus, wavelets allow detecting cyclic oscillations with a floating period, amplitude, and localization (in fact, this is a localized spectral analysis). The choice of the wavelet function is determined by the requirements for spatial and temporal resolutions (sensitivity to changes in the spectral properties of $f(t)$) and, in the case of constructing a discrete basis, the requirement for orthogonality of the resulting basis. In the above example that constitutes the basis of the widely used Morlet wavelet, an analysis with a large σ value corresponds to a higher frequency resolution but loses in the accuracy of localization of the epoch to which the result is attributed on the time axis. By decreasing σ, we sacrifice the spectral resolution of the decomposition but know more precisely to what time instant the obtained spectrum belongs. This circumstance is quite similar to the uncertainty principle in quantum mechanics.

In various fields of science, an analysis of spatial fields with a complex multi-scale structure or signals with time-varying changes in spectral composition is needed (in many cases, the two problems are related). This requirement stimulated attempts to construct special functional expansions using one basis or another, each function of which is characterized both by a certain spatial (temporal) scale and by the place of its localization in physical space (in time). The idea of using short-wave packets to analyze seismic signals when both the burst time and the scale of the signal need to be distinguished was actively developed by Jean Morlet, whose meeting with Alexander Grossmann led to the birth of wavelets. The term itself was introduced in [3], where the main definitions were formulated and the fundamental theorems proved. The work aroused great interest. The mathematical aspects of wavelet analysis have been extensively developed since the late 1980s; by the early 1990s, wavelet analysis had become a popular area of mathematical physics, where it finds wide application for dealing with the problems of time signal analysis, image pattern recognition and synthesis, encrypting and decrypting information, etc. The first informative applications of wavelet analysis in physics date back to the mid-1980s. There is extensive literature on wavelet analysis. Its mathematical aspects are exposed in the fundamental study by Yves Meyer [4], awarded the 2017 Abel Prize for his contribution to the theory of wavelets, and in a number of books by disciples of Alexander Grossmann, including Ingrid Daubechies [5], Matthias Holschneider [6], Bruno Torresani [7], and Stephane Mallat [8]. Despite the voluminous literature on the mathematical aspects of wavelet analysis and its diverse applications, a review of modern wavelet-based methods and results obtained with their help may be useful for observers, experimenters, and signal processors.

Over the past 20 years, a suite of techniques has been developed that is important and necessary for addressing various physical problems. The purpose of the present review is to generalize the experience with the application of wavelet analysis in various fields of physics, familiarize researchers with practical aspects of this application, and propose original wavelet algorithms. In this context, it is important to mention specialized reviews for physicists (in the broad sense of the word, for the 'users' of analytical mathematical methods), including the very first one [9]. Reference [10] proved very useful for Russian readers. *Physics–Uspekhi* has returned repeatedly to this topic in a number of articles [11–13]. A great deal of time has elapsed since the publication of some of them, while others are devoted to rather special problems. The authors of the present publication happened, by the will of fate, to be involved in wavelet research from the first years after its initiation (within the framework of work on turbulence modeling [14], which falls beyond the scope of this review), then gradually expanded the area of the successful application of wavelets, delving deeper into already 'trodden' problems. For example, Ref. [15] was one of the first studies on astronomy in which the wavelet transform was used to search for quasi-periodicities. It is symbolic that the same problem was substantially reinterpreted in the most recent publication [16]. Despite a wide choice of reviews and special articles, we find it appropriate to offer the reader our understanding of the wavelet language as

[1] As with many classical results, the names of other outstanding scientists, e.g., Einstein and Kolmogorov, are associated with this theorem.

a universal tool for the analysis and interpretation of physical signals in multiscale systems.

2. Basic concepts of wavelet analysis

The wavelet analysis arsenal contains a large set of tools that are selected depending on the task of the study and characteristics of the signal. Not claiming to be a general and complete presentation, this section will focus on basic definitions and properties of wavelet analysis, making it an intuitive approach to the interpretation of complex signals.

The starting point of any wavelet research is, as a matter of fact, expansion of the function under study in a suitable wavelet basis, which combines two important properties: pronounced localization in physical and Fourier spaces and similarity. Locality on both sides of the Fourier transform presupposes regularity, i.e., the absence of discontinuities (inevitably contributing to high frequencies) and the equality of the average value (zero frequency) to zero. The latter property is also called the admissibility condition, which explains the appearance of the correction in the real part of a Morlet wavelet:

$$\psi(t) = \exp\left(-\frac{t^2}{\sigma^2}\right)\left(\exp(2\pi i t) - \exp(-\sigma^2\pi^2)\right). \qquad (2)$$

The family of wavelet functions is generated from the analyzing wavelet $\psi(t)$ (also termed 'mother' wavelet function) by two similarity transformations: dilating (compressing) and translating supplemented by rotation in a multidimensional case.

The continuous wavelet transform introduces, by analogy with the Fourier transform (1), the wavelet image

$$w(\tau, t') \equiv W_{\tau,t'}\{f\} = |\tau|^{\kappa}\int_{-\infty}^{\infty} f(t)\psi^*\left(\frac{t-t'}{\tau}\right)\mathrm{d}t, \qquad (3)$$

defined in the space of two independent variables, time t' and scale τ. The preference is given to the latter parameter τ having the meaning of a period rather than frequency (as in the Fourier transform), so that both parameters have the same units of measurement. Parameter κ determines normalization, the choice of which is postponed until the end of this section.The wavelet coefficient $w(\tau, t')$ should be interpreted as a characteristic of the amplitude (and the phase if ψ is a complex quantity) of oscillations of the analyzed function with a characteristic period τ in the vicinity of time instant t'. In this case, it is necessary to take into account that the accuracy of localization in the time-frequency space is finite and predetermined by the choice of wavelet. The resolution $\psi(t)$ of frequency Δ_ω and time Δ_t is defined as the variance of a random variable if normalized functions $|\psi(t)|^2$ and $|\hat{\psi}(\omega)|^2$ are regarded as probability density functions. The effective area of the time-frequency window for any ψ is limited by the Heisenberg uncertainty principle $\Delta_\omega\Delta_t \geqslant 1/2$ [17]. Thus, the choice of a wavelet can be considered an optimization problem.

The normalization index κ is used to relatively enhance (weaken) high (low) frequencies and to adapt the analysis to specific problems when one is interested in some special measure to compare the intensities of differently scaled structures. When analyzing multidimensional signals in (3), a multidimensional integral has to be taken, but (even more importantly) an additional parameter responsible for wavelet anisotropy should be considered, and an additional variable needs to be introduced (as a rule, a positional angle; see Section 4).

An increase in the dimension of the parameter space indicates a redundancy of the received information, the presentation of which requires optimization. The wavelet spectrogram of a one-dimensional signal is the distribution of the modulus of function w (less often, its square is drawn) on the plane (τ, t'). When a complex wavelet is used, the phase of the function w also carries useful information. As a rule, the distribution of the phase on the plane (τ, t') is not considered, but the phase in itself can be of primary interest, e.g., in the search for correlated components in a pair of signals (see Section 2.3).

Leaving aside a review of the wavelet functions used, the popular real wavelet known as the 'Mexican hat', $\psi(t) = (1-t^2)\exp(-t^2/2)$, should be mentioned. Due to its good localization in the physical space, this wavelet is used to highlight individual bursts in the signal. Note also that the Daubechies functions [5], finding wide application, e.g., in commercial software packages, are intended first and foremost for the discrete wavelet transform that is little used in signal structure analysis; therefore, they are not considered in this review.

A signal (or any of its components) can be reconstructed from $w(\tau, t')$ by the inverse wavelet transform:

$$f(t) = \frac{1}{C_\psi}\int_{-\infty}^{\infty}\mathrm{d}\tau\int_{-\infty}^{\infty}\mathrm{d}t'\,\psi\left(\frac{t-t'}{\tau}\right)\frac{w(\tau, t')}{|\tau|^{3+\kappa}}. \qquad (4)$$

The quantity C_ψ plays the role of normalization of the wavelet basis and is calculated as

$$C_\psi = \int_{-\infty}^{\infty}\frac{|\hat{\psi}(\omega)|^2}{|\omega|}\,\mathrm{d}\omega. \qquad (5)$$

The inverse wavelet transform is possible only if C_ψ has a finite value which implies the admissibility condition for a wavelet $\hat{\psi}(0) = 0$. For some frequently used wavelets, C_ψ is found analytically, e.g., $C_\psi = \pi$ for the 'Mexican hat' and $C_\psi = \ln 2$ for the Shannon wavelet $\psi(t) = (\sin 2\pi t - \sin\pi t)/(\pi t)$; for the Morlet wavelet, C_ψ can be found only approximately, since integral (4) of the function $\exp(\mathrm{i}\omega t - \sigma t^2)$ diverges (see Eqn (2)).

The necessity of integration (4) over the region of negative τ values arises in the analysis of complex-valued signals $f(t)$ (see the example in Section 5.2). For real $f(t)$, one can restrict oneself to positive τ. As far as the variable t' is concerned, it is necessary to, formally speaking, integrate over the entire range, whereas integration for real signals is carried out over the region for which observational data are available (bearing in mind boundary distortions that appear as the analyzing wavelet goes outside the region).The inverse transform taken over a certain subdomain of the plane (τ, t') can be regarded as a filtering procedure with a wide choice of bandwidth.

In practice, it is important to be sure that the admissibility condition is satisfied not only for an analytically given ψ but also for its numerical representation. In the analysis of minimal scales, only a few points can fall on the wavelet localization region, and the numerical average for such a limited sample can differ greatly from zero. Problems can arise with the real part of the wavelet (2) when using $\sigma \lesssim 1$ (the fulfilment of the admissibility condition for the imaginary

part is ensured by its odd symmetry). To improve the convergence of integral (5), it can be useful to require the vanishing of the mean value not only of the wavelet itself but also of its several derivatives. The admissibility condition means that the function being analyzed is restored during the reverse transformation with an accuracy up to the mean value. Whenever it is required to restore the average value of the signal, it needs to be calculated separately and then added to what formula (4) gives.

Without going into the mathematical calculations behind the main properties of the wavelet transform, here is an important consequence of Parseval's energy conservation theorem:

$$\int_{-\infty}^{\infty} \left|f(t)\right|^2 \mathrm{d}t = \frac{1}{C_\psi} \int_0^{\infty} \int_{-\infty}^{\infty} \left|w(\tau, t')\right|^2 \frac{\mathrm{d}\tau\, \mathrm{d}t'}{\tau^{3+2\kappa}}. \tag{6}$$

To recall, the power spectral density in a Fourier analysis is the quantity $E(\omega) = |\hat{f}(\omega)|^2$ and the quantity

$$M(\tau) = \int_{-\infty}^{\infty} \left|w(\tau, t')\right|^2 \mathrm{d}t', \tag{7}$$

characterizing the intensity of *all* pulsations of a given scale, is introduced. Assuming $\kappa = -1/2$ in the definition of the wavelet transform (3) allows formula (6) to be rewritten as

$$E = \int_0^{\infty} E(\omega)\, \mathrm{d}\omega = \frac{1}{C_\psi} \int_0^{\infty} M(\tau) \frac{\mathrm{d}\tau}{\tau^2}. \tag{8}$$

In this case, $M(\tau)$ describes the distribution of the pulsation energy over scales and is called the integral wavelet spectrum. It follows from the above that normalization $\kappa = -1/2$ should be used if the results of the wavelet analysis are supposed to be compared with the Fourier representation of the signal. Indeed, if a Fourier spectrum obeys the power law $E(\omega) \sim \omega^\alpha$, then (with this normalization) the integral wavelet spectrum follows the same power law $M(\tau) \sim \tau^{-\alpha} \sim \omega^\alpha$ (this ensues from formula (8), taking into account that $\omega \sim 1/\tau$ and $\mathrm{d}\omega \sim -\mathrm{d}\tau/\tau^2$). Note, also, that the integral wavelet spectrum is always a smoothed version of the Fourier spectrum, with the degree of smoothing determined by the spectral resolution of the wavelet being used.

All subsequent stages of wavelet analysis are based on the subsequent post-processing of $w(\tau, t')$ and the presentation of the information contained in it as dictated by the objectives of the study. In this regard, the integral wavelet spectrum $M(\tau)$ is a useful starting point for research but nothing more than a maximum reduction of the information contained in $w(\tau, t')$.

2.1 Examples of wavelet spectrograms of modulated oscillations

The practical use of the wavelet transform implies, compulsorily, the study of spectrograms. For relatively regular signals, this is of undoubted interest. Any good book or scientific presentation on wavelets includes a demonstration of test signals. The selection of tests usually emphasizes peculiarities of the problem and reflects the logic of subsequent argumentation. The simplest but very instructive tests have been repeatedly described in the scientific and methodological literature (see, for instance, [6, 8, 18]). We propose to consider a series of three examples:

$$\begin{aligned} f_1(t) &= \sin\left(\frac{2\pi t}{20}\right)\left(1 + \frac{t}{500}\sin\left(\frac{2\pi t}{125}\right)\right), \\ f_2(t) &= \sin\left(\frac{2\pi t}{20}\right) + \sin\left(12\pi \exp\left(\frac{t}{400}\right)\right), \\ f_3(t) &= \sin\left(\frac{2\pi t}{20} + \left(1 + \frac{3t}{500}\right)\sin\left(\frac{2\pi t}{200}\right)\right); \end{aligned} \tag{9}$$

the spectrograms for them illustrate manifestations of nonstationary amplitude or frequency modulations. It can be noted that these functions include a common harmonic with a period of 20 onto which various distortions are superimposed: $f_1(t)$ is the amplitude modulation of the harmonic function linearly growing in time with a period of 125; $f_2(t)$ is the additive component with an exponentially decreasing period selected so that the periods of the two components coincide in the middle of the interval; $f_3(t)$ is the frequency modulation according to the harmonic law with a period of 200 and a linearly increasing amplitude. Each modulation leads to a deformation of the uniform band corresponding to the wavelet image of a purely harmonic function.

Graphs of the analyzed functions and their wavelet spectrograms are presented in Fig. 1. All three signals are

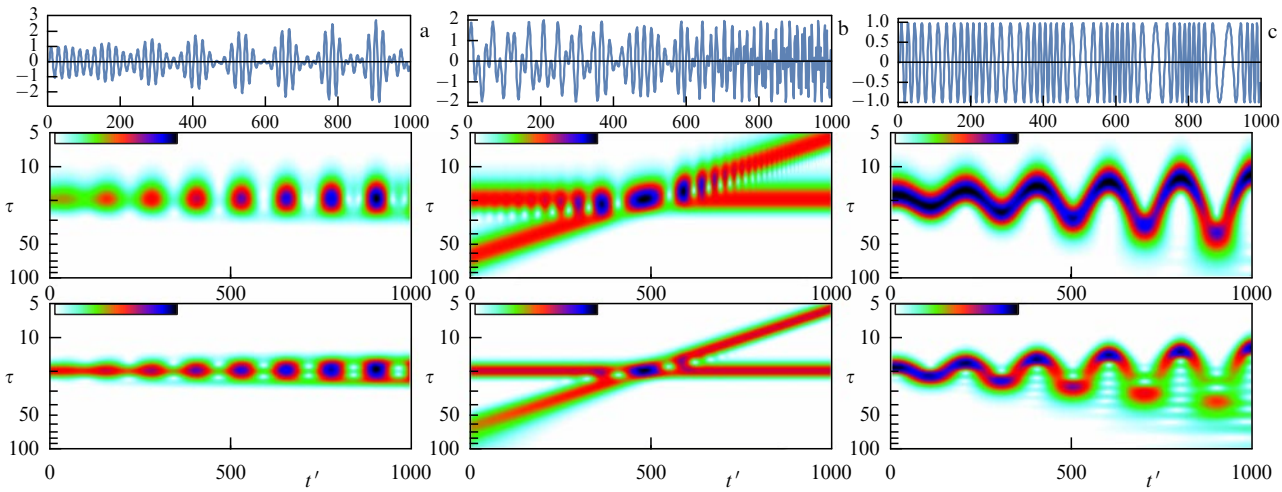

Figure 1. (Color online.) Test signals f_1 (a), f_2 (b), and f_3 (c) (top row), wavelet spectrograms $|w_1|$ (a), $|w_2|$ (b), $|w_3|$ (c) at $\sigma = 1$ (middle row) and at $\sigma = 2$ (bottom row).

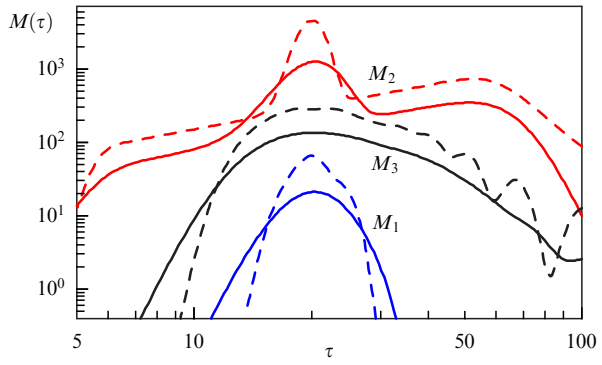

Figure 2. (Color online.) Integral wavelet spectra of test functions f_i: M_1 — blue curves, M_2 — red, M_3 — black. $\sigma = 1$ — solid curves, $\sigma = 2$ — dashed curves. $M_i(\tau)$ spectra are vertically shifted for better perception.

processed by wavelet (2) with two values of the parameter σ. A rise in σ increases the spectral resolution, i.e., produces narrower bands on the spectrograms (bottom row in Fig. 1). In the case of relatively good localization in the physical space (at $\sigma = 1$), the wavelet image w_1 exhibits a well apparent tendency toward an increase in the amplitude of the carrier oscillations. The spots on the wavelet image w_2 correspond to the beats resulting from superposition of oscillations with similar periods. This effect builds up closer to the middle of the interval. If the resolution in the physical space is reduced in favor of the scale resolution ($\sigma = 2$), the periodic components become better isolated, and oscillations can be seen at the periods corresponding to the half-sum and the half-difference of the fundamental and modulating frequencies. However, an increase in σ can compromise the informative value of the wavelet image. It is better to track frequency modulations f_3 at small σ. When there is poor localization in the physical space, relatively fast modulations in the long-wavelength region are blurred.

The selection of test signals is such that integral wavelet spectra, like the Fourier spectra, can not reflect their features. Nevertheless, they are presented in Fig. 2 in order to illustrate sensitivity to the main stationary component. For f_1 and f_2, the contribution predominates on a scale of 20, while, for f_3, it is markedly smeared in the interval conditioned by the modulation amplitude.

2.2 Wavelet differentiation

The problem of the numerical differentiation of an approximately known function is a classic example of an ill-posed problem that leads to instability of the solution [19]. To ensure stability, the exact solution is replaced by an approximate one which is controlled by a certain regularization parameter and tends to be accurate in the absence of measurement errors. In practice, regularization usually reduces to either smoothing the original data in physical space or suppressing high frequencies in the spectrum of the measured data. In this case, the optimal width of the smoothing window or the corresponding filter bandwidth is associated with the expected noise level.

The fundamental difference between the Fourier differentiation algorithm and direct differentiation in the physical space boils down to the following: calculation of the Fourier transform requires the use of information about the signal at all points of the numerical axis, while differentiation is, by definition, a local operation.

The problem of regularization of the procedure for noisy data differentiation is naturally formulated in the language of wavelet representation of signals, which allows combining advantages of the operation in physical space and Fourier space [20].

Let the function $f(t)$ have the first derivative $g(t) = \partial f/\partial t$ and be defined on the set of points t_n up to some random errors ξ ($\tilde{f}_n = f(t_n) + \xi_n$). The wavelet transformation of the function $g(t)$ and differentiation by parts readily lead to

$$W_{\tau,t'}\{g\} = \tau^{\kappa} \int_{-\infty}^{\infty} \psi^* \left(\frac{t - t'}{\tau} \right) g(t)\, \mathrm{d}t = -\tau^{\kappa-1} \int_{-\infty}^{\infty} \psi'^* \left(\frac{t - t'}{\tau} \right) f(t)\, \mathrm{d}t\,. \qquad (10)$$

In other words, the wavelet image of the derivative of $f(t)$ can be obtained without direct calculation of the derivative of the initial data. The derivative $g(t)$ itself is obtained by reconstruction from its wavelet image, making use of the inverse wavelet transform (4). In fact, the procedure for numerical differentiation of f_n is substituted by numerical integration and analytical differentiation of a given family of wavelet functions. Note that $\psi'(t)$ should also meet all the requirements for wavelets.

2.3 Scale-by-scale cross-correlation of signals

An analysis of the behavior of complex systems consists not only in following the course of evolution of the spectral composition of a certain signal but also in studying the degree of correlation between two signals separately on each time scale. The potential of Fourier analysis in this situation is very limited. The Fourier cross-spectrum,

$$E_{ij}(\omega) = \hat{f}_i(\omega) \hat{f}_j^*(\omega)\,,$$

can be introduced, which, by itself, by virtue of the equality $|E_{ij}|^2 = E_{ii} E_{jj}$, does not carry additional information. A partial solution to the problem was proposed by introducing coherence [21]

$$\gamma(\omega) = \frac{\overline{E_{ij}(\omega)}}{\left(\overline{E_{ii}(\omega)}\, \overline{E_{jj}(\omega)}\right)^{1/2}}\,, \qquad (11)$$

where $\overline{(\cdot)}$ denotes a smoothing operation. The quantity $\gamma(\omega)$ varies over the range from 0 to 1, with 1 corresponding to the linear relationship between the oscillation intensities at a given frequency in both signals. It should be noted that the choice of the filter width $\overline{(\cdot)}$ must be justified separately.

The language of wavelets makes it possible to naturally formulate characteristics of the correlation between signals localized in the space of scales and time. The energy distribution on the cross-spectrogram $C_w(\tau, t') = w_1(\tau, t') w_2^*(\tau, t')$ (see, for instance, Fig. 3) highlights the scales and time ranges in which oscillations appear simultaneously in two signals. In this case, the inherent principles of maintaining the optimal resolution in the scale-time space make the interpretation of the results of analysis more confident. The idea of wavelet cross-correlation analysis was first proposed in connection with the comparison of variability of various solar characteristics [22]. The wavelet cross-correlation function of two signals was defined as

$$C_{12}(\tau) = \frac{\int C_w(\tau, t')\, \mathrm{d}t'}{\left(\int w_1^2(\tau, t')\, \mathrm{d}t' \int w_2^2(\tau, t')\, \mathrm{d}t' \right)^{1/2}}\,, \qquad (12)$$

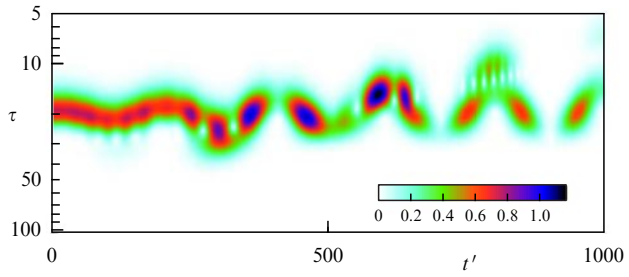

Figure 3. (Color online.) Cross-spectrogram of f_2 and f_3 signals.

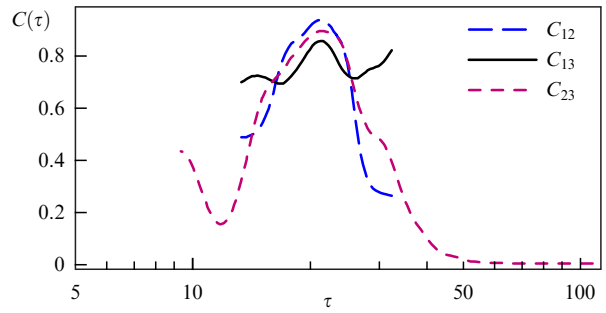

Figure 4. (Color online.) Wavelet cross-correlations of test functions (9).

where w_1 and w_2 are the wavelet images of the signals under consideration. The absolute value of $|C(t')|$ characterizes the degree of consistency of the occurrence of oscillations with scale t' in two signals, while the phase $\delta\phi_{12} = \arg(C_{12}(\tau))$ shows the average phase shift between them. Pairwise wavelet correlation functions for the previously considered test signals (9) are shown in Fig. 4. It can be seen that they reach a maximum at $\tau = 20$. In this case, the cross-correlation coefficients for test signals are equal to 0.56 between f_1 and f_2, -0.04 between f_1 and f_3, and 0.02 between f_2 and f_3.

By analogy with characteristic (11), one can consider wavelet coherence [23]

$$\Gamma(\tau, t') = \frac{\overline{w_{ij}(\tau, t')}}{\left(\overline{w_{ii}(\tau, t')}\;\overline{w_{jj}(\tau, t')}\right)^{1/2}}\,, \tag{13}$$

where the smoothing operation, for example, with a moving average, is carried out in the plane (τ, t'). Then, the function $C(\tau)$ is a special case of $\Gamma(\tau, t')$ where $\overline{(\cdot)}$ is averaging over t'. Based on $\Gamma(\tau, t')$, it is possible to construct a wavelet coherence spectrogram displaying the cross-correlation coefficient and the magnitude of the phase shift localized in the scale-time space. $\Gamma(\tau, t')$ is used most effectively to analyze chaotic signals with a wide range of scales [24, 25].

It is worth mentioning the generalization of the wavelet correlation method proposed in [26, 27] for the case of several time series. The correlation is introduced as a matrix product of wavelet transforms of the corresponding series. Then, the peak in the correlation function appears only at the frequency present in each of the processed series.

2.4 Wavelet analysis of signals with gaps

Let us consider the algorithm proposed for solving a fundamental problem that arises in the processing of observational and (less often) measurement data, i.e., the problem of inevitable gaps (holes) in the series due to a variety of reasons. For example, many stars observed in a given observatory are only above the horizon part of the year but remain invisible for the rest of the time. This happens for the same reason that the Sun is not visible at high latitudes during the polar night. Although it is possible, in principle, to combine data from observatories located at different latitudes, it is a very difficult task; therefore, data on stellar activity are usually available only for a certain part of the year (during the so-called observational seasons; see the example in Fig. 16). These problems gain importance in the analysis of cycles of stellar activity, because the total duration of observations (at best, several ten years) is insufficient to cover more than a few cycles. An analysis of the spectral composition of such signals faces serious problems which can be mitigated using the wavelet algorithm proposed in the context of research on cyclicity of stellar activity [28]. The mathematical substantiation of the algorithm is proposed in Ref. [29].

Let us turn now to the signal $f(t)$ registered with gaps, i.e., when one knows, instead of $f(t)$, the function

$$\tilde{f}(t) = f(t)G(t)\,, \tag{14}$$

where $G(t)$ is the 'gap function' equal to one if the signal is recorded and to zero at all other points (inside the gaps and outside the signal). As a result, the calculation of the wavelet coefficients yields, instead of the sought $w(a, b)$ values, coefficients

$$\tilde{w}(\tau, t') = W_{\tau,t'}\{\tilde{f}\} = \tau^{\kappa}\int_{-\infty}^{\infty}\psi^*\left(\frac{t-t'}{\tau}\right)\tilde{f}(t)\,\mathrm{d}t\,. \tag{15}$$

The idea behind the algorithm called gapped wavelets is to transfer the problem of gaps from an unknown function $f(t)$ to the well-known function ψ. Let us rewrite formula (15) as a convolution of the original function $f(t)$ with a 'gapped' wavelet:

$$\int_{-\infty}^{\infty}\psi^*\left(\frac{t-t'}{\tau}\right)\tilde{f}(t)\,\mathrm{d}t = \int_{-\infty}^{\infty}\tilde{\psi}^*\left(\frac{t-t'}{\tau}\right)f(t)\,\mathrm{d}t\,,$$

where $\tilde{\psi}[(t-t')/\tau] = \psi[(t-t')/\tau]G(t)$.

Falling on gaps, the function $\tilde{\psi}$ ceases to satisfy the requirements for wavelets, in particular $\int\tilde{\psi}(t)\,\mathrm{d}t \neq 0$. It is proposed to replace the 'corrupted' wavelet $\tilde{\psi}$ by the 'corrected' ψ_{g}, which must at least satisfy the condition $\langle\psi_{\mathrm{g}}\rangle = 0$ and tend toward the original wavelet ψ as gaps disappear. In the language of Fourier representations, the following interpretation of the proposed idea can be given. A peculiar feature of wavelets is that their Fourier image is localized in a limited frequency band. Violation of the condition $\langle\psi\rangle = 0$ leads to the appearance of frequencies as low as $|\hat{\psi}(\omega)|^2$ in the $\omega \to 0$ spectrum, while discontinuities at the edges of holes produce high-frequency noise. It is necessary to specify an algorithm that suppresses both low- and high-frequency noise caused by gaps and edges (considered to be semi-infinite gaps).

To implement this idea, the wavelet ψ is represented in the form

$$\psi(t) = h(t)\Phi(t)\,, \tag{16}$$

where $\Phi(t)$ is the positive definite scale function (the 'envelope' usually used as the Gaussian function $\Phi(t) = \exp(-t^2/2)$) and $h(t)$ is the 'filling' function (the parabola for the 'Mexican hat', the complex harmonic function for the Morlet wavelet).

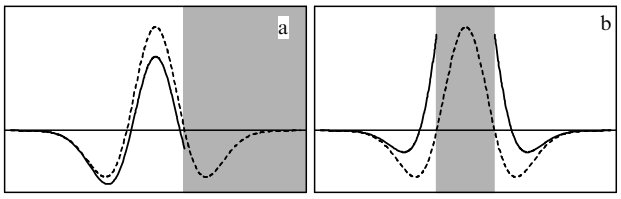

Figure 5. Examples of corrections of an analyzing wavelet in processing a signal fragment with gaps (a — at the edge, b — at a single gap). Gaps are shown in gray, dashed curve denotes the original wavelet, solid curve is the correction result.

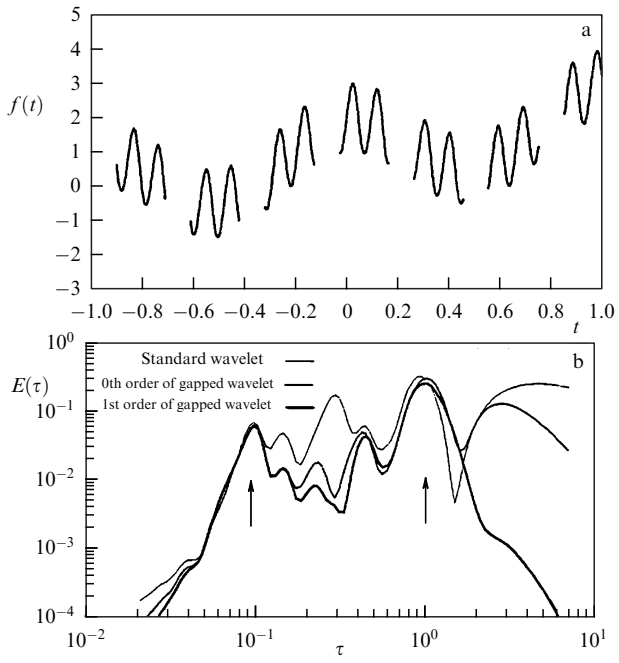

Figure 6. Model signal with gaps (a) and its wavelet spectra (b); standard wavelet transform (thin line), gapped wavelet (bold line). (Adapted from [29].)

The desired wavelet ψ_g is sought in the form

$$\psi_g(t) = \big(h(t) - H\big)\Phi(t)G(t)\,. \tag{17}$$

The quantity H is determined for each scale τ and position of the center of wavelet t', based on the condition $\langle\psi_g\rangle = 0$; it equals

$$H(\tau, t') = \frac{\int_{-\infty}^{\infty} h\big(t - t'/\tau\big)\Phi\big(t - t'/\tau\big)G(t)\,\mathrm{d}t}{\int_{-\infty}^{\infty} \Phi\big(t - t'/\tau\big)G(t)\,\mathrm{d}t}\,. \tag{18}$$

The character of the change in the wavelet at the edge and in a single gap is shown in Fig. 5. The 'Mexican hat' shown by the dotted curve is taken as the analyzing wavelet $\psi(t)$. Cases of maximum deviation of the mean value from zero are presented: in the first case (Fig. 5a), the edge completely cuts off one wing; in the second one (Fig. 5b), the gap exactly covers the entire central maximum (in the figure, these regions are shown in gray). It can be seen that, even in these situations, the structure of the function undergoes no critical changes. New functions $\psi_g(t)$ (solid line) have discontinuities that coincide with the boundaries of the gaps and do not introduce additional noise during integration. Figure 6 exemplifies the calculation of the wavelet spectrum of a model signal with gaps. Figure 6a shows the analyzed signal, and Fig. 6b, its wavelet spectra calculated using the standard wavelet algorithm (thin line) and with the help of gapped wavelets (bold line). The spectrum of the original signal must contain two peaks, the positions of which are indicated by arrows. It can be seen that the standard technique reveals a false peak, associated with gap systematicity, and significant low-frequency noise. In the corrected spectrum, not only is the false maximum markedly suppressed, but also the positions of the main maxima correspond much more accurately to the original frequencies in the signal.

It should be noted that the algorithm requires large computational resources, since it includes the calculation of two additional convolutions in (18), but these costs are justified in the analysis of signals with numerous gaps or short signals for which the influence of edge effects can be critical. The possibility of accelerating calculations based on fast wavelet transform algorithms was considered in [30].

3. Wavelets for the search and study of quasiperiodicities

3.1 Cycles of solar activity

One of the most challenging physical problems to be solved with the use of wavelets is the identification and the analysis of quasiperiodicities in various time series obtained in the course of laboratory, nature, or astronomical observations. Perhaps the most discussed issue of this kind concerns the results of long-term observations of solar cyclic activity, among which the data on the sunspot numbers occupy an important place (see, for example, [31, 32]). Indeed, astronomy in the context of exploration of the Solar System is one of those areas of knowledge in which the modern system of physical and mathematical sciences was formed. Sunspots have attracted people's attention since antiquity, but their instrumental studies go back to 1611 when Galileo first used a telescope for astronomical observations. It is hardly possible to find a time series of instrumental investigations or measurements longer in real astronomical time.

It is well known (see, for example, Ref. [33] for an overview) that the evolution of solar activity includes quasiperiodic components. Indeed, the sunspot numbers increases and reaches a maximum roughly every 11 years; thereafter, it decreases and falls to a minimum. This is the famous 11-year cycle of solar activity that attracts public attention and leads scholars representing various disciplines to discuss how this phenomenon affects different aspects of human life, down to the intensity of drug use or wheat prices. One cycle of activity may differ slightly from the previous and subsequent ones both in duration and in intensity. At the turn of the 17th and 18th centuries, the sunspot numbers was significantly smaller than in other observation periods known to researchers. This gave rise to the concept of a global minimum in solar activity that was called the Maunder minimum after the English astronomer who had been the first to explore this phenomenon. In addition to sunspots, there are other tracers of solar activity, some of which are associated with the dynamics of radioactive isotopes in various objects. Isotope tracers make it possible to more or less successfully follow the dynamics of solar activity over much longer time intervals, up to 10,000 years [34]. These data indicate that global minima, similar to the Maunder minimum, have occurred more than once in the past, with their

sequence showing no obvious pattern. All the above features of solar activity make it a very convenient and interesting material for wavelet analysis. This is probably why one of the first studies devoted to the use of wavelets to search for and study quasiperiodicities in astronomical data was focused on the analysis of sunspot observations [15].

A time series analysis spanning hundreds of years encounters a number of specific problems typical of many areas of physics that, as a rule, have to do with what is happening right now and can be, in principle, reproduced many times. If the length of a given time series significantly exceeds both the typical time of active action of an individual observer and the typical time needed to significantly improve an observational technique, then difficulties arise in compiling a time series that aims to have at least some level of homogeneity. Certainly, the first telescopes were much less sophisticated than modern ones, and the sunspot observation technique required some time to be developed. Nevertheless, the known examples show that there were conscientious and diligent people among the very first observers whose studies were of pleasantly surprising quality. At the same time, modern research practice funded largely by grants does not encourage long-term projects that stipulate decades of homogeneous routine observations. All this makes the problem of relevant compilation of time series of a specific solar activity tracer somewhat similar to the one of describing historical events based on data from various sources. Hence, one has to talk about one reconstruction of time series or another [35]. Such problems are not directly related to wavelet analysis, although it can also help in stitching data obtained by two observers that partially overlap in time. These aspects of the problem are not discussed in the present review (see [36] and [37] for details); instead, some data on the average monthly number of sunspot groups recorded from 1611 to 1996 are presented [38]. More recently, a thorough revision of these data was undertaken in Ref. [39], which provided a basis for calibrating results of different observers [40, 41]. We collected these data together and obtained a series remarkable in that it includes the Maunder minimum as well as the most recent time period (after 1996). In these years immediately preceding the present time, the behavior of the Sun was very unusual. Although solar activity was apparently not as weak as it had been during the Maunder minimum, it resembled a less pronounced episode of decreased activity known as the Dalton minimum that occurred during the Napoleonic wars.

Presenting results of a wavelet analysis of a generalized data set, we follow the authors of Ref. [15] that was one of the first studies on the use of wavelets in astronomy and astrophysics. However, we recalculated these results for a modern dataset. Moreover, the early methods made it possible to use only time series with the data evenly spaced apart from each other in time, while the database contained small gaps that had to be interpolated. Today, it is not necessary to do due to the use of the gapped wavelet technique.

Figure 7 shows the analyzed time series, and Fig. 8 is a wavelet spectrogram of the number of sunspot groups according to the daily resolution data for the periods from 1610 to 1739 (Ref. [38]) and from 1739 to 2010 (Ref. [41]) and according to the monthly resolution data obtained since 2010 [42]. This is the longest series of the number of sunspot groups to date. A bright stripe corresponding to the nominal 11-year cycle is well apparent. Directly during the Maunder

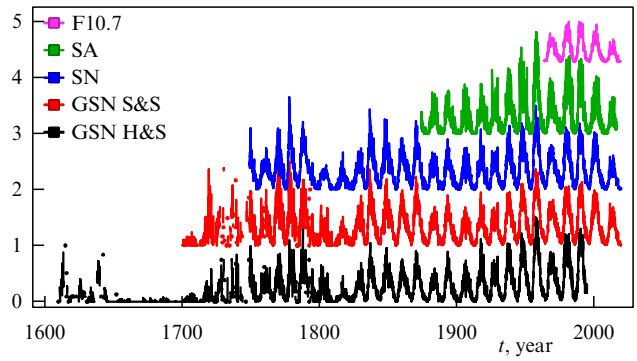

Figure 7. (Color online.) Analyzed solar activity data with monthly averaging: number of sunspot groups according to well-known study [38] (designated GSN H&S) and the respective data with deep processing, recalibration [40], and the addition of modern data [42] (GSN S&S), sunspot number (SN) according to SILSO (http://www.sidc.be/silso/datafiles), sunspot area (SA) according to Royal Greenwich Observatory (https://solarscience.msfc.nasa.gov/greenwch.shtml), and solar irradiance index at 10.7 cm (F10.7) according to OMNIWeb (https://omniweb.gsfc.nasa.gov).

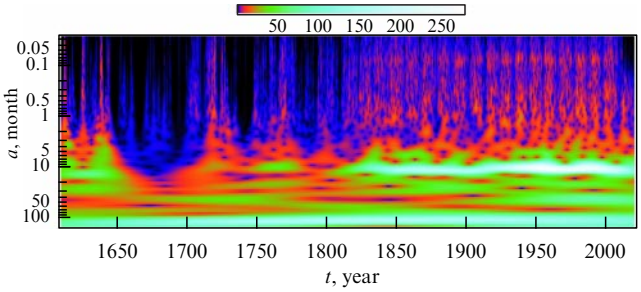

Figure 8. (Color online.) Wavelet spectrogram of sunspot groups.

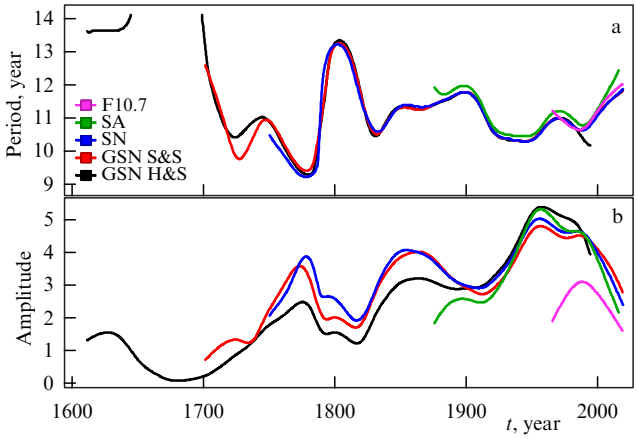

Figure 9. (Color online.) Characteristic period τ^* (a) and amplitude w^* (b) of the 11-year cycle.

minimum, the bright line is interrupted, which means that the analyzed time series (at least within the framework of spectral analysis) does not indicate the presence of the Schwabe cycle at this time. Of course, the possibility remains that in this epoch a cycle existed but for some reason did not manifest itself in the form of observable sunspots; for example, magnetic tubes did not float at all or the spots were so small that they escaped the attention of observers.

A wavelet spectrogram can be used to quantitatively track changes in the parameters of the solar cycle. Figure 9 shows

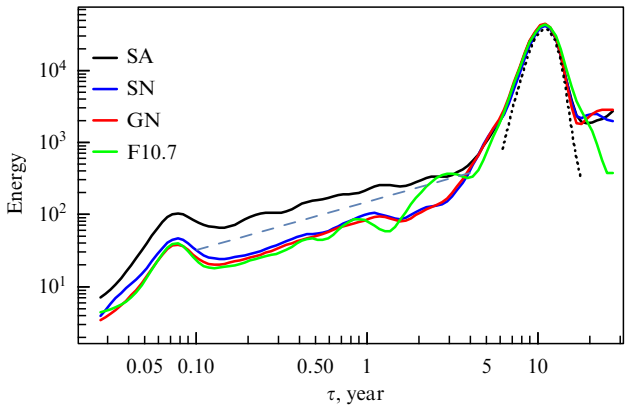

Figure 10. (Color online.) Global wavelet spectra for different tracers in the interval of $0.02 < \tau < 20$ years. Dashed line denotes $\tau^{2/3}$ slope. Dotted line shows the expected response from the 11-year sine signal. (From [16]).

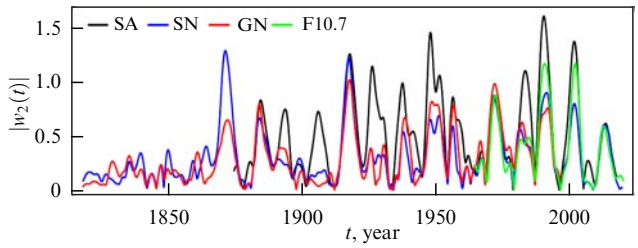

Figure 11. (Color online.) Variations in amplitude of two-year quasiperiodicity ($w(\tau = 2, t')$) for various tracers. (From [16].)

the evolution of the characteristic period τ^* and the amplitude w^* of the main cycle of activity which are determined by the maximum intensity at the current time instant, $w^*(t') = |w(\tau^*, t')| = \max_\tau |w(\tau, t')|$. Clearly, if the epoch near the Maunder minimum is disregarded, the length of the Schwabe cycle varies from cycle to cycle, but in general these variations are small. It seems natural to associate them with statistical fluctuations of the parameters that determine the operation of the mechanism underlying self-excitation of the magnetic field (solar dynamo) [43, 44].

Let us now turn to variations in the number of sunspot groups and other similar tracers with a characteristic time of less than 11 years [16]. Figure 10 shows in these time scales an extended range of a continuous spectrum typical of many problems arising in the study of turbulent and convective flows. As is known, the investigation of such phenomena initiated by Richardson constitutes the central idea of Kolmogorov's turbulence theory. On the other hand, the idea of so-called quasi-biennial cycles is widespread in solar physics [45]. Practically any period in the interval between 1 and 4 years was regarded as a possible duration of these cycles, and the terminology itself suggests that this phenomenon is not quite similar to the 11-year Schwabe cycle. Variations of activity were also detected during observations of stars (see Section 3.2), but the observable time series of stellar magnetic activity are much shorter than analogous time series for the Sun. This makes the problem of separating phenomena similar to the Schwabe cycle and quasi-biennial oscillations much more difficult to approach. It is known that a statistical analysis of individual rare events can reveal the reaction of global chaotic systems, such as terrestrial and space climate, to weak external influences [46].

This problem is even more challenging in the search for physical mechanisms maintaining solar and stellar cycles. It is now generally accepted that the physical cause behind the Schwabe cycle is the self-excitation of a magnetic field wave as a result of the combined action of differential rotation and mirror-asymmetric convective turbulence even if details of this solar dynamo remain to be elucidated (see, for example, [47]). In any case, a subject of the discussion is the appearance of a eigen oscillation in the linearized equations describing this phenomenon. A noticeable complication of this model gives reason to consider self-excitation of a magnetic field in two layers of the convective shell, say, near the surface and at the bottom of the convective zone of the Sun. It is also possible to reach excitation of eigen oscillations in these shells with significantly different periods, although it is likely to raise the unpleasant question of how the traces of such oscillations occurring far inside the Sun penetrate to its surface and why regions in the parametric space where such a phenomenon occurs turn out to be dangerously narrow. The prospect of explaining the whole set of periods in a similar manner seems utterly unattractive, and understanding quasi-biennial oscillations as elements of a continuous convective spectrum appears to be a natural solution to this problem.

Let us see, following the authors of Ref. [16], how methods of wavelet analysis help to clarify this problem. Integral (global) wavelet spectra of variations among four activity tracers for the time interval from 1875 to 2019 (or part of it in the absence of relevant data for the entire period) are presented in Fig. 10. Each spectrum has two well apparent maxima, one corresponding to the Schwabe cycle, the other close to the solar rotation time. A natural interpretation of the second maximum attributes it to the fact that the lifetime of some sunspots exceeds the solar rotation time due to which they are seen several times and are therefore recorded in the database more than once. An integral wavelet spectrum exhibits a continuous power-law range between the two maxima that are typical for turbulent systems. One can be convinced of the stochastic nature of oscillations with a roughly 2-year cycle by considering the dependence $w(\tau = 2, t')$ (Fig. 11). Evidently, quasi-biennial oscillations differ significantly between tracers and vary markedly in time.

Assuming some additional distinguished periodicity in solar activity spectra even if it changes with time, one has to accept the requirement that the corresponding fluctuations must be expressed during at least several solar cycles. Cutting out various temporal sections of the wavelet plane, it is possible to obtain a wavelet spectrum on the scale of a concrete solar cycle. Figure 12 shows oscillation spectra of twelve separate solar cycles (from the 13th to the 24th). To facilitate perception, the spectra are normalized to $\tau^{2/3}$. Also, individual cycles are artificially shifted vertically relative to each other.

It can be seen that only two peaks survive in all cycles, while the spectral composition of each one changes from cycle to cycle in the absence of stable features. Local maxima in individual cycles appear in a range of scales from $\tau = 0.2$ to $\tau = 4$ years. Figure 12b shows the height of the local maxima found in the spectrum of an individual cycle relative to the nearest local minima. Two high maxima can be recognized at $\tau = 2$ (in the cycle $N = 16$) and $\tau = 2.7$ (in the cycle $N = 23$) years. There are many other slightly less significant maxima that occur evenly in the mid-term. Figure 12c presents integral compensated spectra and the respective confidence intervals obtained from the statistics of realiza-

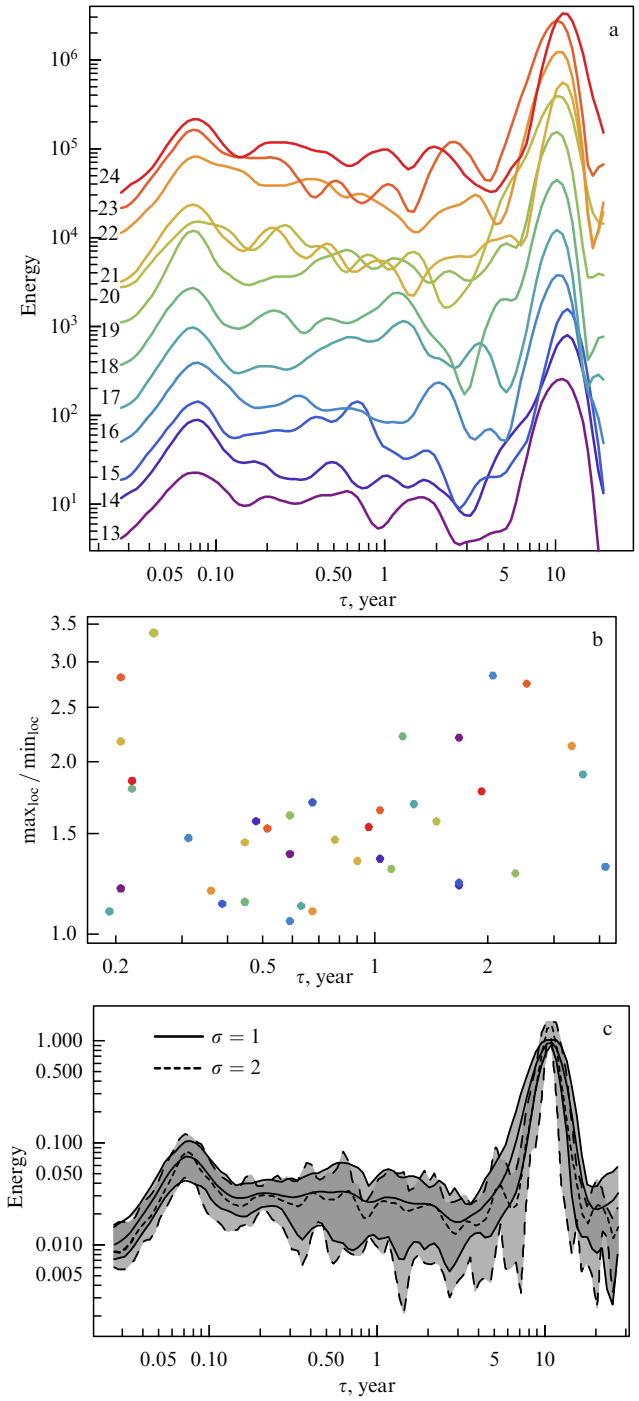

Figure 12. (Color online.) (a) Wavelet spectra for individual cycles compensated by $\tau^{2/3}$ and evenly shifted vertically for better visualization. (b) Local maxima for individual cycles. (c) Wavelet spectrum averaged over 12 cycles. Gray shading represents two-sided confidence interval of 80%. Solid and dashed lines correspond to result obtained at different values of the wavelet parameter: $\sigma = 1$ and $\sigma = 2$, respectively. (From [16].)

tions in separate cycles. It can be seen that fluctuations of various durations (less than 11 years) occur in concrete cycles, whereas stable fluctuations of more or less constant duration are absent.

Thus, the wavelet analysis revealed pronounced fluctuations with time scales from several months to 11 years in each individual cycle and showed that their random contributions give a smooth common spectrum. At large τ, deviations from

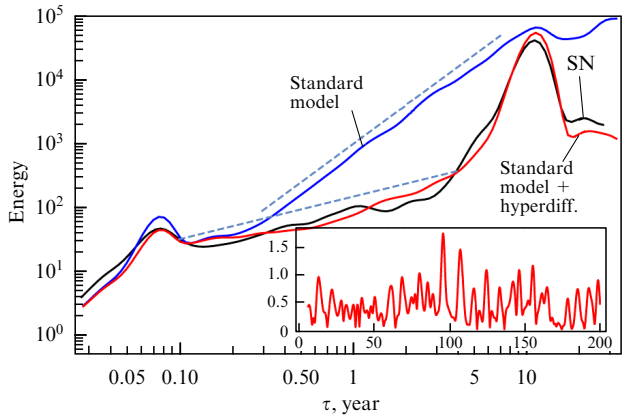

Figure 13. (Color online.) Wavelet spectra for SN (black curve) and two simulation signals: (blue) standard dynamo model (see [49]) and (red) same model with the hyperdiffusion effect. Dashed lines denote 2 and 2/3 slopes. Inset shows evolution of the wavelet amplitude of two-year quasiperiodicity. (From [16].)

the $\tau^{2/3}$ law become more pronounced, which can be attributed to poor statistics within individual cycles. This may be a manifestation of strong intermittency of the dynamo process as indicated by direct calculations of variations in the scaling characteristics [48].

Finally, it is worth noting the results of simulations of the structure of activity spectra in the framework of a simple solar dynamo model [49] that includes the formation of sunspots. In this context, there is no need to insist that this particular model most adequately describes the solar cycle. It is more important that building the model does not involve embedding physical mechanisms barring those that lead to the Schwabe cycle.

Figure 13 shows results of a wavelet analysis of the simulated database in comparison with real data. It can be seen that the variation in the parameters of the model which lies within the permissible limits makes it possible to rather accurately reproduce the real wavelet spectrum of a given tracer. On the whole, the analysis performed allows the conclusion that the available data give reason to understand quasi-biennial oscillations as elements of a continuous spectrum, the physical nature of which differs from that of the Schwabe cycle.

A comparative analysis of wavelet-based processing measurement data and mathematical modeling opens up wide opportunities for constructing a consistent picture of a physical phenomenon. Recently, special attention has been paid to experimental and theoretical studies of the sources of magnetohydrodynamic (MHD) oscillations and waves in the atmosphere of sunspots (see review [50]). It is possible to single out the analysis of the dynamics of propagating wave fronts in the active zone for the spatial resolution of which the method of pixel-by-pixel wavelet filtering was developed [51–53].

The idea of wavelet cross-correlation analysis arose from comparing the variability of various solar parameters [22]. The fact is one more characteristic of the Sun (apparent solar diameter) was constantly measured in the era of the famous Maunder minimum, the adjective ‘visible’ being a key word; changes in this parameter do not necessarily mean changes in the physical size of the Sun but can be a mere optical effect. Variations of the apparent solar diameter were continuously recorded by astronomers of the French school from 1683 to

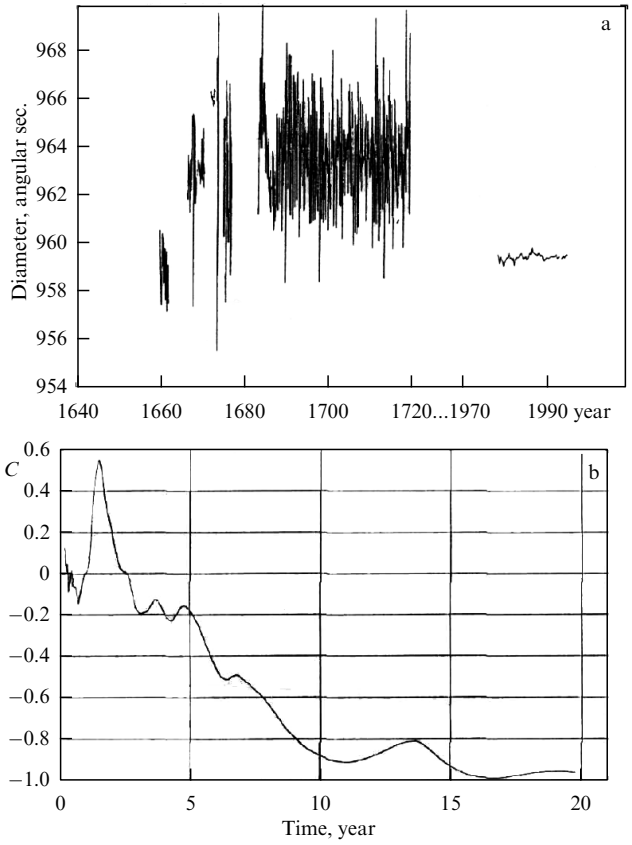

Figure 14. (a) Variations in apparent solar diameter according to historical sources (before 1720) and modern data [54]. (b) Wavelet cross-correlation of variations in the apparent solar diameter and the number of sunspot groups. (From [22].)

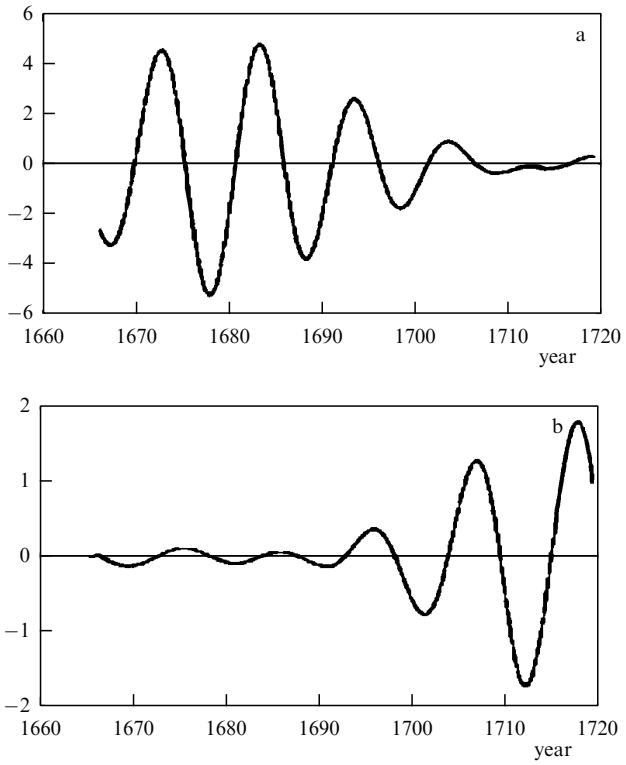

Figure 15. 11-year fluctuations extracted from data on variations in apparent solar diameter (a) and the sunspot group numbers (b). (From [22].)

1718, and separate series of measurements had been carried out by various astronomers even earlier. Systematic observations of this characteristic were resumed only in 1974 [54]. All available measurement results are collected in Fig. 14a. There is a striking difference between modern data and those obtained 400 years ago. A simple explanation of this fact is that the quality of measurements in the distant past was much lower than in the present day, which accounts for the high level of signal pulsations (the systematic difference in the signal level is explained by the fact that the apparent diameter of the Sun is a subjective value depending on the method of measurement). However, wavelet analysis shows that it is hardly possible to ascribe the said difference to measurement errors, and these archival data contain useful information.

Figure 14b shows the correlation function (12) calculated for variations in the sunspot group numbers and the Sun's diameter over overlapping observation intervals. It can be seen that, at times on the order of 2 years, there is a narrow positive peak, and, at time scales of the order of 10 years or more, signals become strictly anti-correlated (the more spots, the smaller the diameter).

Of greatest interest is the frequency of the main (11-year) solar cycle. Filtered curves of 11-year variations in the diameter and sunspot group numbers for the time interval of 1666–1718 are presented in Fig. 15. It is noteworthy that observations of changes in the solar diameter began during the Maunder minimum and continued during the outcome from it. The results of wavelet filtering of observational data presented in Fig. 15 show that the 11-year variations in solar diameter had the greatest amplitude just during the deep minimum of solar activity. By the end of the minimum, variations in the sunspot numbers began to increase, while variations in the diameter decreased. This finding gives a hint to explain the striking difference between the modern data and those obtained in the 18th century. The mean sunspot group numbers increased by about an order of magnitude in comparison with 1718, when measurements of solar diameter were stopped. In light of these observations, this should lead to a significant reduction in the intensity of variations in the diameter documented by modern researchers.

The result obtained opens up the possibility to conclude that the Maunder minimum is not magnetic but hydrodynamic in nature. Of course, one has to be cautious when making conclusions based on delicate archival observations, but it is clear that calculations of the correlation using wavelets give more confidence.

3.2 Cycles in stellar data

The cyclic activity of the Sun is not a unique phenomenon; it is equally inherent in other stars having physical characteristics more or less similar to those of the Sun. Indeed, astronomers have observed and investigated the cyclic activity of various stars by different techniques for about half a century (see, for example, [55]). To recall, one of the main methods used in these studies, so-called inverse Doppler imaging, was developed in our country [56]. It makes possible mapping the temperature distribution over the surface of a variety of stars. Stellar activity research not only is interesting in and of itself but also contributes to a better understanding of solar activity. For example, it was recently found out that powerful flares that occur on some stars having characteristics similar to those of the Sun would bring danger to our modern

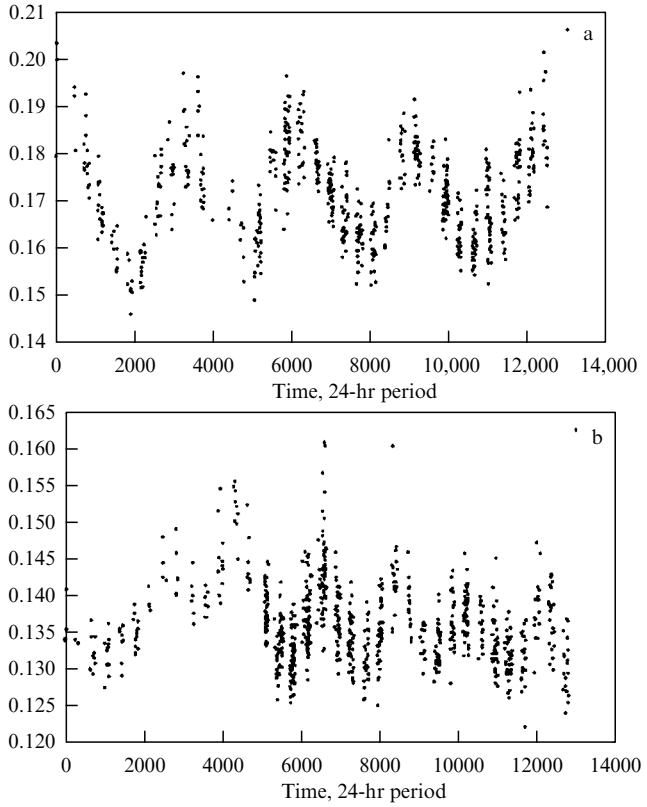

Figure 16. Examples of observational data on the chromospheric activity of two stars: HD81809 (a) and HD161239 (b).

technological civilization if they happened closer to Earth (see [57] for details). Fortunately, there is still no immediate threat to Earth and there is some difference between the properties of stars with powerful flares and those of the Sun. In general, however, such studies are not only of cognitive interest.

Figure 16 presents, by way of example, data on the chromospheric activity of two solar-type stars exhibiting pronounced cyclicity. They fairly well illustrate problems related to stellar observations, such as relatively short series that comprise only a few oscillations of the main cycle, existence of numerous gaps (seasonal observations) and a high level of noise of unknown origin (the nature of the star's radiation, properties of the interstellar medium, or observation conditions).

Due to the limited size of this review, it is not intended to compare cyclicity in the activity of different stars, and the interested reader is referred to the literature ([28, 58, 59]). What follows will illustrate the usefulness of wavelet analysis not only for studying global and local spectral properties but also for elucidating more subtle characteristics of periodic or quasi-periodic signals.

Let us consider the method proposed in the context of these problems and called by the authors Double Wavelet Analysis (DWA) [58, 60]. The idea of the method is to introduce a parameter that characterizes the deviation of the shape of the stellar cycle from that of the harmonic one. The Morlet wavelet in the form (2) is used as the analyzing wavelet; its adjustable parameter σ determines the spectral (spatial) resolution. If the analyzed signal is a periodic sequence of relatively short bursts, then, at a large value of parameter σ (high spectral resolution), the fundamental frequency is readily apparent together with multiple harmonics; the higher the burst duty cycles, the greater the number of such harmonics. At small σ (e.g., $\sigma = 0.3$), the wavelet (2) has the form of a single burst and resolves each oscillation, the trace from which on the wavelet plane stretches toward high frequencies (small scales), the maximum energy going far away from the fundamental frequency in proportion to the burst narrowness. The latter circumstance prompted the introduction of a measure of signal deviation from the harmonic determined as the distance between the maximum and the fundamental frequency.

The algorithm is as follows. Initially, the wavelet transformation of the analyzed periodic (quasiperiodic) function $f(t)$ is carried out, and a Morlet wavelet with a good spectral resolution ($\sigma > 1$) is used to find the scale (characteristic period) of the main oscillation T_c with good accuracy from the maximum in the wavelet spectrum $M_0(\tau)$.

Next, the first step of the double analysis is performed, during which the wavelet coefficients are recalculated with a small σ that ensures good temporal resolution,

$$w_1(\tau, t') = W_{\tau, t'}\{f\}\,. \tag{19}$$

The second step (repeated wavelet transformation) is intended to reveal at what time scale the fundamental frequency appears best. To this end, a wavelet analysis of the field $w_1(t')$ is carried out for each τ value and calculations are made only for one fixed scale T_c:

$$\begin{aligned} w_2(\tau, t) &= W_{T_c, t}\{w_1(\tau, t')\} \\ &= a^{-1/2}\int |w_1(\tau, t')|\psi\left(\frac{t' - t}{T_c}\right) \mathrm{d}t'\,. \end{aligned} \tag{20}$$

At this stage, a good spectral resolution is again required, i.e., $\sigma > 1$. Finally, the DWA-spectrum is calculated:

$$M_2(\tau) = \int_{-\infty}^{\infty} |w_2(\tau, t)|^2\,\mathrm{d}t\,. \tag{21}$$

The narrower individual bursts in the signal, the farther the spectral peak M_2 moves away from the position of the main peak in the initial wavelet spectrum M_0. The quantity

$$A = \frac{T_c}{\tau^*} \tag{22}$$

is introduced as the anharmonicity parameter, with T_c being the scale of the main cycle calculated at the first step and τ^*, the time scale (period) with which the maximum energy in the M_2 spectrum is associated. For the harmonic signal $A = 1$, the larger the parameter A, the more the time series resembles a pulsating signal.

For the data presented in Fig. 16, wavelet spectra M_0 (thin lines) and M_2 (bold lines) are shown in Fig. 17 (with an arbitrary vertical shift). In both cases, the M_0 spectra clearly show a maximum corresponding to the main stellar cycle (2900 and 1900 days, respectively). The middle part of the spectrum displays a burst near 365 days revealed by seasonal observations. The high-frequency part of the spectrum of the star HD81809 exhibits a small maximum on a scale of 40 days; it is the period of the star's revolution (fluctuations in the radiation intensity are due to the uneven distribution of active regions over the surface of the star).

Two specific features of the M_2 spectra should be emphasized. First is a pronounced shift of the main maximum observed in both stars. The anharmonicity parameter

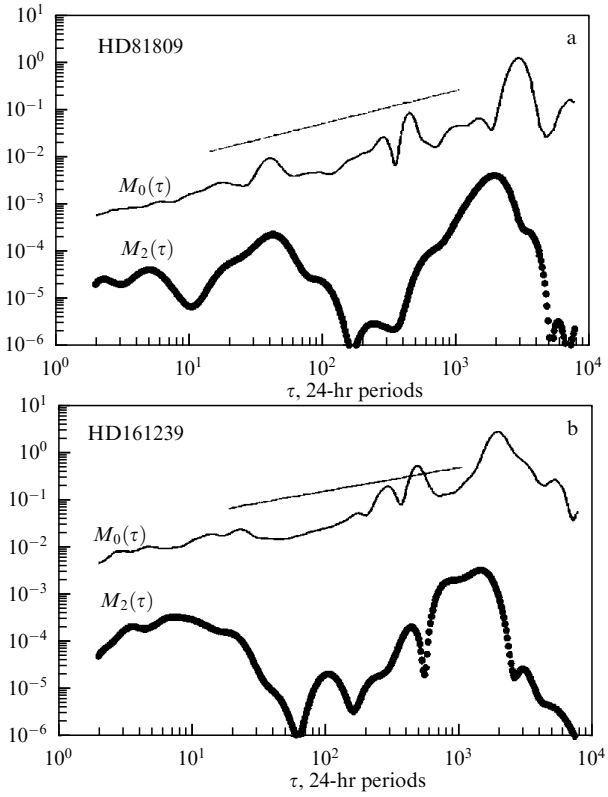

Figure 17. Results of processing observational data on the chromospheric activity of the stars HD81809 (a) and HD161239 (b). Wavelet spectra of initial data (thin lines) and spectra obtained after double wavelet analysis (bold lines). (Adapted from [58].)

for them has the values $A = 1.5$ and $A = 1.3$ (A values for various stars lie in a range from 1.0 to 5 [59]). Second, a repeated wavelet transformation gives rise to the dominance of two peaks in the spectra: the expected main one and the one corresponding to the star's rotation period.

Thus, the method of double wavelet analysis allows identifying a weak high-frequency periodic signal (rotation) in the presence of a pronounced low-frequency component. This method of measuring the rotation period of a star can be compared to tuning a radio receiver in order to obtain optimal sound quality: by rotating the radio receiver's tuning knob (in analogy with searching frequencies in the M_2 spectrum), one is looking for a frequency at which the loudness of the useful low-frequency signal (cyclicity of stellar activity) is maximum. Finding the maximum is equivalent to determining the frequency of the transmitting radio station (the period of rotation of the star).

In certain cases, this method made it possible to distinguish the rotation period even in the absence of its trace in the spectrum of the initial signal [58]. For the star HD161239, the double wavelet analysis gave a rotation period of 7 days, whereas other sources estimate the period of rotation of this star at 10 or 23 days in the absence of a pronounced peak associated with the rotation period in the M_0 spectrum.

Note that Refs [61, 62] proposed an identical algorithm with a similar name, 'the double wavelet approach', but intended to be used under different approaches according to different goals and sequences of actions. In this method applied to analyze systems with two significantly different dominant frequencies, a high frequency is first allocated, and

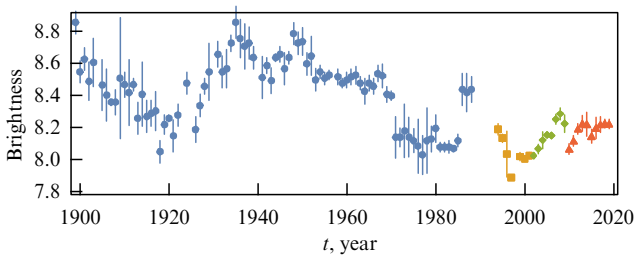

Figure 18. Long-term variations in average annual brightness of the star V833 Tau, the minimum values of which correspond to maximum activity (largest number of stellar spots). Sources of observational data and approaches to their unification are described in detail in Ref. [64].

a doubled transformation is used to study the processes causing high-frequency modulation.

It is important that observations of stellar activity allow only integral radiation to be registered. The aforementioned mapping is carried out by comparing the integral signals obtained at many wavelengths and at different times. Therefore, isolation of the rotation frequency of the star in the spectrum of integral radiation means that regions with increased or decreased radiation intensity appear on the surface of the star, and the lifetimes of these regions (structures) should exceed the star's revolution time. In addition, stars, like almost all nonsolid rotating space objects, are characterized by differential rotation (the angular velocity of rotation is not uniform over both the latitude and the radius). This means that active regions are responsible for variations in total radiation with different frequencies (variations in angular velocity can reach 20%). The authors of [63] proposed a method for estimating the degree of rotation differential from the results of wavelet analysis of a star's integral radiation. The fact is that, if a signal contains two close frequencies and the spectral resolution of the wavelet is insufficient to separate them, then beats appear on the wavelet plane (see Fig. 1). The essence of the method in [63] is that optimization of the spectral resolution of the wavelet by choosing the parameter σ in formula (2) leads to a noticeable beat effect, and the beat frequency is used to estimate frequency spread, i.e., scattering of angular velocities of rotation of individual regions located at different latitudes.

The last example of wavelet processing stellar data considered in this review concerns the recent results of an analysis of emission from the star V833 Tau [64]. This star is interesting for two reasons: the unprecedented duration of observations of the star (about 120 years) and the complicated time dependence of radiation allowing a variety of interpretations. It is easy to see (Fig. 18) that, depending on the length of the period chosen to observe the overwhelming majority of stars (usually several decades), V833 Tau exhibits a qualitatively different behavior. This example allows a general remark that the observation of 10 characteristic times of evolution of a single star can be more valuable than the observation of one characteristic time of 10 different stars. In the literature, the quasiperiodicity of V833 Tau is described as compound; namely, oscillations with periods of 78.25, 18.8, 6.4, and 2.5 years are distinguished [65]. The wide range of permitted scales makes it possible to raise the question of the extent to which oscillations with these periods are isolated and dominate over the others. Alternatively, oscillations of V833 Tau can form a continuous

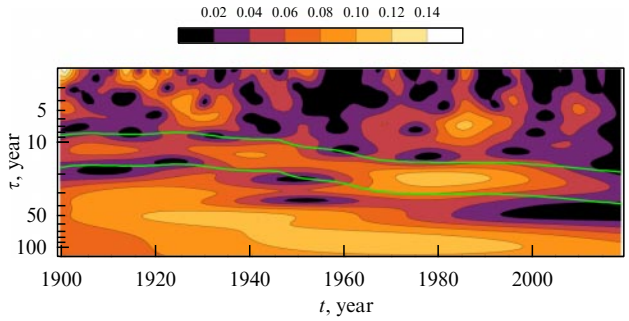

Figure 19. (Color online.) Wavelet spectrogram of the magnetic activity of V833 Tau ($|w(\tau, t')|$ at $\kappa = -1$). Green lines show the range of scales in which fluctuations are tracked for further reconstruction. (From [64].)

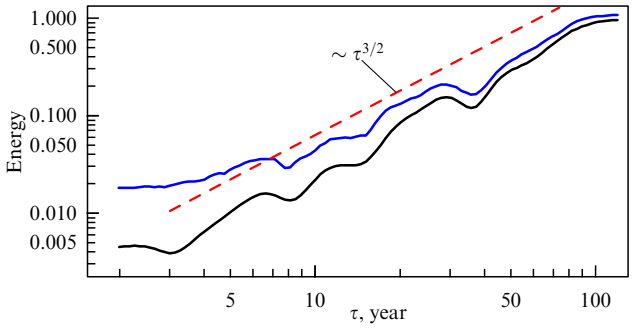

Figure 20. (Color online.) Integral wavelet spectrum for V833 Tau (black curve). Blue curve shows the upper limit of the confidence interval (0.9). (From [64].)

turbulent spectrum by analogy with the way the quasi-biennial oscillations of solar activity are interpreted in Section 3.1.

The wavelet spectrogram of V833 Tau in Fig. 19 demonstrates a wide variety of multiscale oscillations. To begin with, there is no bright band present on the spectrogram of the Sun (see Fig. 8). With some caution, one can distinguish several structures, between the scales of 10 and 40 years, where the action of the stellar dynamo can be expected. In the area marked with green lines, one can notice some connectivity of the structure (peaks) in time. An integrated wavelet spectrum based on the V833 Tau data is shown in Fig. 20. On the one hand, there is no pronounced local maximum that could be qualitatively compared with the maximum in the solar spectrum (see Fig. 9). In the vicinity of $\tau \approx 30$, there is a jump which is the contribution of vibrations within the band identified in the spectrogram. A Monte Carlo simulation can be performed using the standard error shown by the bar for each data point in Fig. 18 to estimate the upper bound of the confidence interval (Fig. 20 shows the level for a probability of 0.9). It is seen that the maximum at $\tau = 30$ is not sufficiently significant. On the other hand, the integral wavelet spectrum of V833 Tau can be described by a power law with $\tau^{3/2}$. The short-term part of the spectrum ($\tau \lesssim 10$) is likely to be affected by noise, but the remaining part is relatively statistically stable. Fluctuations in the activity of V833 Tau in the range $3 < \tau < 100$ can be compared with the behavior of fluctuations in solar activity observed on a scale of $0.1 < \tau < 10$. Then, it seems natural to assume that if V833 TAU has a solar-type dynamo cycle, its period is 10 times longer than that of the solar dynamo. However, the available data are insufficient to isolate it.

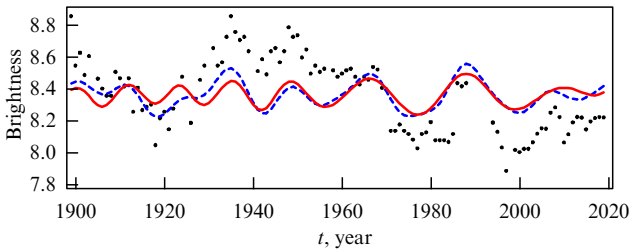

Figure 21. (Color online.) Variants of reconstruction of the main cycle of the star V833 Tau: reconstruction from wavelet coefficients between the green lines in Fig. 19 (red curve) and from the fixed scale range $10 < \tau < 40$ (blue dashed curve). Original data are denoted by black dots. (From [64].)

Interestingly, V833 Tau is a rather young and very active star with a rotation period of less than 2 days, which suggests a high degree of saturation of the dynamo process. Such a stellar dynamo regime is characterized by a quasi-stationary magnetic field with chaotic variations. A discussion of all theoretical premises can be found in [64]. Here, it will be shown only how, with the help of the inverse wavelet transform, the dynamo cycle of V833 Tau can be distinguished in the search for oscillations comparable to 11 years of the solar cycle. The standard approach available for any filtering method is to leave the signal contained in some dedicated range of scales. Within the framework of the wavelet analysis, the time scale of the signal is revealed, which makes it possible to track transition processes. Figure 21 shows two possible reconstructions, one of which is performed using wavelet coefficients in a fixed range of scales $10 < \tau < 40$ (blue dashed line) and the other, in the adaptive band shown in Fig. 19. The most significant difference is apparent in the interval between 1920 and 1930 where the blue dashed curve has a phase failure, while the characteristic scale of the oscillations shown by the red curve is noticeably reduced and does not lose its oscillatory character. Such behavior once again emphasizes the difference between the observed variations in V833 Tau and solar activity (see the wavelet analysis of the Schwabe cycle phase in [66]).

3.3 Wavelet analysis of climatic and geophysical data

The earth sciences are perhaps the most popular area of application of wavelet analysis, which is especially widely used in the fields of climatology, terrestrial magnetism, and solar-terrestrial relations. The number of studies using wavelets for this purpose amounts to thousands, and even a cursory review of them would be difficult to perform and hardly interesting without highlighting a specific physical problem. Therefore, this section is confined to illustrating the potential of the method. From the standpoint of wavelet analysis, most studies can be categorized into two groups. The first deals with the analysis of variability of certain characteristics and the identification of cyclicity in a variety of forms. Studies in the second group are concerned with the analysis of spatial and/or temporal correlation of signals of different natures for the purpose of identifying their relationships and the physical mechanisms underlying them.

The first group includes numerous studies on the analysis of observational data, from the simplest quasi-periodic processes (seasonal variations) to more complex ones (El Niño and others), from the search for traces of weak periodic influences (those of satellites, planets, etc.) to aperiodic

processes such as earthquakes and tsunamis or variations in the polarity of the geomagnetic field, separation (filtration) of periodic changes, and long-term trends.

The second group includes articles on the analysis of solar-terrestrial relationships (the search for correlations between geophysical signals of various natures and solar activity), correlations (often not obvious) among the variabilities of the most varied climatic and geophysical characteristics in different parts of the planet, and identification of the anthropogenic impact on the environment.

As far as the first group of studies is concerned, the restoration of data on Earth's climate change is not only of scientific but also of obvious practical interest. What is meant are relatively small (of the order of degrees) temperature changes over sufficiently long (at least tens of years) periods of time. At the same time, mean values of Earth's surface temperature are available from instantaneous data recorded by weather stations which vary significantly from place to place, from day to day, and from night to day. Differentiating between global and local, and slow (climate) and relatively fast (weather) variations requires adequate data filtering.

Let us demonstrate the possibility of using the inverse wavelet transform by an example of identifying a long-term temperature trend in temperature data for Central England (the Stratford-upon-Avon region) available since the middle of the 17th century [67]. This is the longest time series of regional data unaffected, as far as possible, by nearby large cities. There are several more time series of approximately the same length containing temperature measurements in individual settlements. A comparison of these data with regional temperature data from Central England by the methods of wavelet analysis is of undoubted interest but lies beyond the scope of this review.

To analyze the longest time series, direct wavelet transformation was carried out and the integral wavelet spectrum considered as a basis for differentiating between short-period (weather in the broad sense of the word) and long-period (climate) temperature variations. The inverse wavelet transformation was performed in the second part. Naturally, it is desirable that the border between weather and climate be expressed as clearly as possible and run along a deep minimum in the integral wavelet spectrum. In reality, however, this minimum (for which a period of about 50 years is taken) is not as deep as one would like. Therefore, the division between climatic changes and weather fluctuations turns out to be somewhat arbitrary, and Fig. 22 shows results of recovery with three upper filtration boundaries: $\tau < 200$ years (*1*), $\tau < 120$ years (*2*), and $\tau < 40$ years (*3*).

Figure 22 shows that the average annual temperature in Central England has indeed been growing since the middle of the 19th century and reached its maximum values today, but at the turn of the 17th and 18th centuries a noticeable decrease in average annual temperatures occurred. This period is sometimes called the Little Ice Age. In general, these results fit into the concept of global warming, but it can hardly be said that they themselves confirm all the details of this concept. As is often the case, even perfect methods for the analysis of data concerning a single tracer do not help to find out everything that interests a researcher.

Considerable experience in using wavelets has been accumulated during studies of variations in Earth's magnetic field. An analysis of quasiperiodicities of the geomagnetic field on scales of hundreds and thousands of years based on

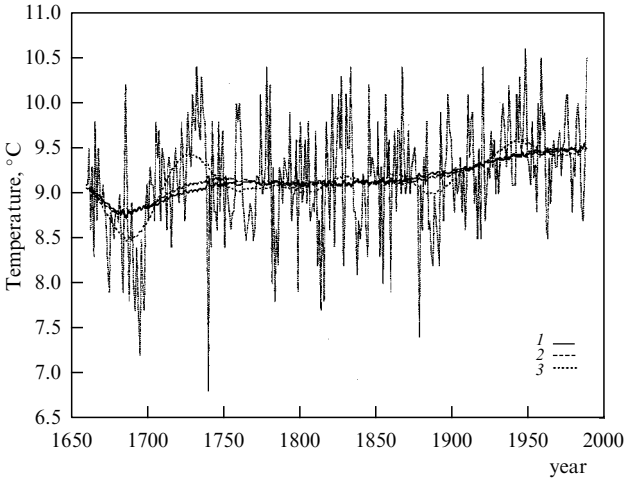

Figure 22. Results of wavelet filtering of temperature variations in central England with different upper bounds: $\tau < 200$ years (*1*), $\tau < 120$ years (*2*), $\tau < 40$ years (*3*) [67].

the results of investigations of sedimentary rocks from various regions on Earth led the authors of [68] to the conclusion that there are no identified scales in the range of 300–4000 years. Note that the conclusion about the absence of allocated frequencies is often no less important than the conclusion about their presence.

Perhaps the longest among time series of observational data in which researchers are trying to find traces of quasiperiodicities is the geomagnetic polarity scale (GPS), which carries information only about the sign of the magnetic field (more precisely, it indicates Earth's hemisphere where the north magnetic pole is located). Today, the standard scale contains hundreds of magnetic field reversals that occurred over the past 250 million years, and prospects for its extension to earlier epochs are being discussed. The very possibility of an adequate assessment of spectral characteristics of a signal only from the results of recording changes of its sign is far from obvious. A wavelet analysis of various model signals of random processes and analogs of the polarity scale constructed from them carried out in conjunction with an analysis of the GPS allowed the authors to assert that, for the low-frequency part of the spectrum (low frequencies in this case include oscillations with a period of more than 1 million years), the exponent γ in the spectrum $E(\omega) \sim \omega^{\gamma}$ is close to unity [69]. Later attempts to find distinguished quasiperiodicities in the polarity scale were undertaken in Ref. [70], which documented the presence of traces of a period of roughly 50 mln years; these traces were compared with the data of geodynamo models [71].

As for wavelet cross-coherence (13), it makes possible singling out nontrivial correlations among observed phenomena. For example, a joint analysis of the North Atlantic Oscillation index and solar activity revealed the quasiperiodic reversal of the coherence sign with a period of about 50 years [72].

An example of the analysis of long-term solar-climatic correlations is provided by a study of temperature and carbon dioxide variations reconstructed from 11,000-year-old Antarctic ice and their comparison with the data on solar activity reconstructed for the same period [73]. A number of coincident peaks were found in the oscillation spectra of all three series, but only oscillations on scales close to 1000 years

showed a stable correlation of temperature and solar activity variations with a stable phase shift. At the same time, the correlation between variations in the carbon dioxide level and temperature turned out to be low and unstable.

An interesting example of spatial correlation analysis is the work on processing archeomagnetic data (estimation of the amplitude of the geomagnetic field during the firing of ceramic items collected by archaeologists in a given region) obtained from three geographic areas: Bulgaria, Georgia, and Central Asia [74]. The data in each group was a nonuniform random sample over the time interval from 2000 BC till now. The spectrum of each sample had a set of peaks, with the peak corresponding to the oscillation period of 1750 years being most pronounced in all three series; the phase shifts at this frequency in all three signals made it possible to identify a wave of perturbations of the geomagnetic field propagating from east to west with a speed of about 0.2 deg/year. In the context of the analysis of spatial correlations of observational data for Earth's magnetic field, it is pertinent to mention work on the analysis of the cross-correlation of data from geomagnetic observatories located at different points on Earth [75].

The vertical component of the geomagnetic field observed in real time by ground-based observatories of the International Network of Magnetic Observatories was used to analyze magnetic fields induced by the motion of tsunamis and the geomagnetic field [76]. The main focus was on small-scale geomagnetic variations caused by the tsunami on February 27, 2010 according to the Easter Island Observatory (IPM) and the Papeete Observatory (PPT). Wavelet analysis and maximum variance analysis (MVA) were used to detect tsunami-related perturbations in geomagnetic data. It was shown that such a combination of the two methods can be used to calibrate tsunami models and apply them in real time to analyze tsunami forecasting scenarios.

4. Wavelet analysis of astrophysical images

Historically, modern physics formed as an experimental science, i.e., a science dealing with relatively simple, somewhat artificial, situations: the ball that Galileo threw from the tower fell not at all like a thin sheet of paper from a window of a house. However, in the course of the development of a specific area of physics, the task of comparing such slightly idealized concepts with a much more chaotic world around us arises sooner or later. For example, one has to fit the ideas of laboratory hydrodynamics into the context of atmospheric or marine physics. To demonstrate the possibilities of and difficulties in using wavelets, we choose problems associated with the study of spiral galaxies using radio astronomy methods. These tasks appear to be especially difficult to address, because people do not have sense organs that can allow them to directly perceive information obtained in radio astronomy. An image produced with an optical telescope can be perceived as an objective reality, at least at the very beginning. On the contrary, a map of, say, polarized radio emission of some spiral galaxy is presented as a set of poorly ordered spots, and significant efforts are needed to make it suitable for scientific analysis by intelligently combining radio data with each other and with the optical image. The relevant terminology itself used in the context of this discussion gives evidence of the presence of spiral structures (so-called spiral arms) in images of spiral galaxies obtained in various tracers. The spiral arms obtained from tracers that visualize the distribution of interstellar gas or stars, as a rule, do not coincide with the arms obtained from tracers that visualize the distribution of magnetic fields. Of course, there are simple examples of situations in which the localization of a particular spiral arm is beyond doubt, but in certain cases one sees, say, two spiral arms upon a quick look at the image but becomes aware of the presence of four and even six of them in the course of further work. The identification of spiral arms and the relationships among them allows understanding what physical processes lead to their formation. To get there, one must learn how to measure the pitch-angle of these arms, which is practically impossible without algorithmically described methods for identifying and quantitatively digitizing these objects.

One more aspect of the problem is of importance. A spiral structure forms not only in relation to the distribution of gas and stars in galaxies but also in association with the magnetic field distribution. Such magnetic fields are observed and measured from the Faraday effect of rotation of the synchrotron radio emission polarization plane as it passes through a magnetized plasma. A classic description of this effect finding application (in a slightly different form) in the sugar industry is given in the book by V L Ginzburg [77]. Usually, there is a medium that simultaneously emits and rotates a wave, and the parameters of the problem are such that it is reasonable to carry out observations in the radio range (the classical wavelength range used in connection with this problem is from 3 to 20 cm). As a result, not only is the plane of polarization rotated, but also the degree of polarization decreases (usually it is not about 70% but roughly 10%). In simple situations, polarization angles ψ of radio emission with different wavelengths λ obey the rule

$$\psi(\lambda) = \psi_0 + \mathrm{RM}\lambda^2\,, \tag{23}$$

where the Faraday rotation measure (RM) is proportional to the strength of the magnetic field, and angle ψ_0 contains information on field direction (see [78] for details). Naturally, we are speaking about observations of radio emission with different wavelengths, i.e., multifrequency radiation.

The first attempt at wavelet-based identification of spiral arms was undertaken in [79]. Images of the galaxy NGC6946 were projected onto the galactic plane and were thereafter broken into concentric rings. Each ring was subjected to one-dimensional wavelet analysis by the azimuth angle, and the positions of local maxima were plotted on a map with circles, the size of which corresponded to the scale of the wavelet. The result for the image of this galaxy in polarized radio emission and in the optical range is shown in Fig. 23. Solid lines in this figure show the results of parameterization of the corresponding structure with a logarithmic spiral. The above images clearly show that the magnetic arms are markedly displaced relative to the gas arms observed in the optical range.

This approach is quite a laborious procedure applicable when the number of objects under study is relatively small and they can be considered individually. In mass observations, in which the amount of observational information is such that it does not allow viewing and thinking over each image individually, it is natural to use two-dimensional wavelets.

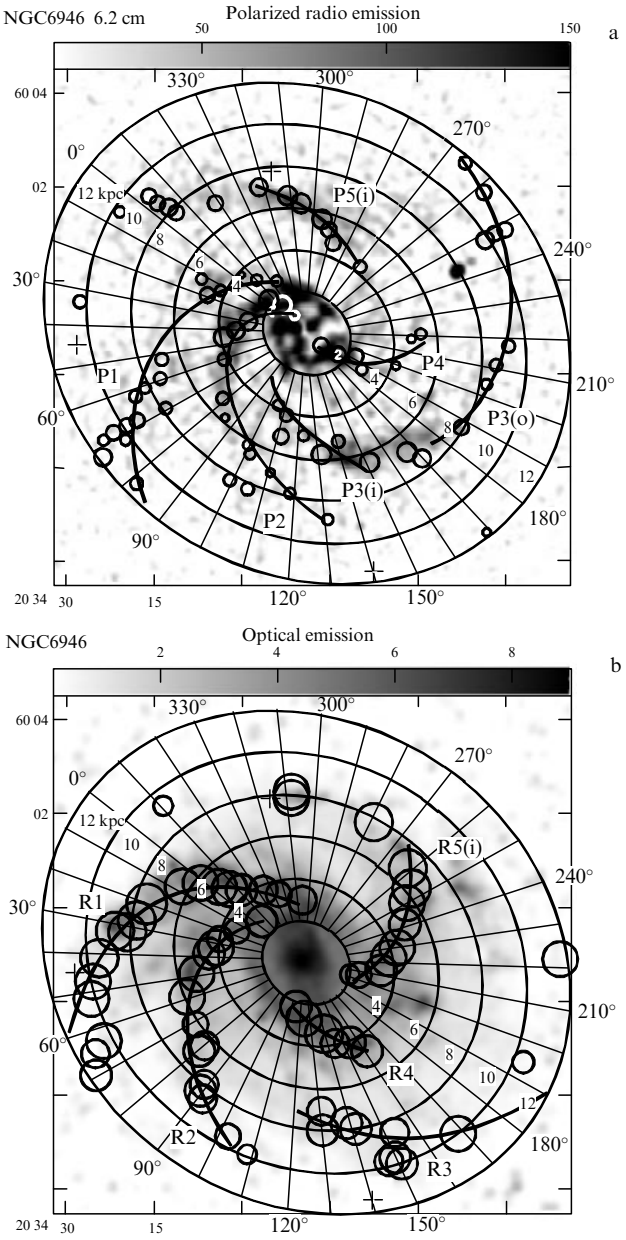

Figure 23. Maps of polarized radio emission (a) and optical radiation (b) of the galaxy NGC6946 with the maxima plotted on them in one-dimensional azimuthal wavelet images. The size of the circles corresponds to the wavelet scale at which this maximum is observed. (From [79].)

4.1 Isotropic analysis

The wavelet image of a two-dimensional function is defined as

$$w(\tau, \mathbf{x}') = \frac{1}{\tau^{\kappa}} \int_{-\infty}^{+\infty} \int_{-\infty}^{+\infty} f(\mathbf{x}) \psi^* \left(\frac{\mathbf{x} - \mathbf{x}'}{\tau} \right) \mathrm{d}\mathbf{x}\,, \tag{24}$$

where the variable τ specifies the spatial scale, $\mathbf{x} = (x, y)$, and $f(\mathbf{x})$ is the analyzed two-dimensional function. The choice of analyzing wavelet becomes even wider: along with simple axisymmetric functions for the analysis of structures, one can use rather complex functions that describe not only wave packets of different types but also special-type structures (e.g., spiral ones) responsible for the appearance of additional conversion parameters. A two-dimensional version of the 'Mexican hat' $\psi(\rho) = (2-\rho^2)\exp(-\rho^2/2)$, $\rho = \sqrt{x^2 + y^2}$, as well as more complex axisymmetric functions that improve the spectral resolution of the wavelet, is widely used as the simplest isotropic wavelet (see, for example, [80]).

The inversion formula for *isotropic* transformation (24) is a natural generalization of formula (4) and has the form

$$f(\mathbf{x}) = \frac{1}{C_\psi} \int_{-\infty}^{+\infty} \int_{-\infty}^{+\infty} \int_{0}^{+\infty} w(\tau, \mathbf{x}') \psi \left(\frac{\mathbf{x}' - \mathbf{x}}{a} \right) \frac{\mathrm{d}\tau}{\tau^{5-\kappa}} \, \mathrm{d}\mathbf{x}'\,, \tag{25}$$

where

$$C_\psi = \frac{1}{4\pi^2} \int_{-\infty}^{+\infty} \int_{-\infty}^{+\infty} \frac{\left|\hat{\psi}(\mathbf{k})\right|^2}{|\mathbf{k}|^2} \, \mathrm{d}\mathbf{k}\,, \tag{26}$$

and $\mathbf{k} = (k_x, k_y)$ is the two-dimensional wave vector.

Before turning to the analysis of the spiral structure, let us discuss the possibilities of statistical analysis of galactic images, including an analysis of spectral density of spatial fluctuations of recorded fields and the correlation of these fluctuations in different fields.

In the wavelet representation, the distribution of the pulsation energy over scales is characterized by the *integral* wavelet spectrum, defined as the average energy of all wavelet coefficients of a given scale τ over the entire plane:

$$M(\tau) = \int_{-\infty}^{+\infty} \int_{-\infty}^{+\infty} \left| w(\tau, \mathbf{x}') \right|^2 \mathrm{d}\mathbf{x}'\,. \tag{27}$$

Wavelet spectrum (27) can be easily related to the Fourier spectrum. In the isotropic case, this relationship has the form

$$M(\tau) = \frac{\tau^{4-2\kappa}}{2\pi} \int_0^{\infty} E(k) \left|\hat{\psi}(\tau k)\right|^2 \mathrm{d}k\,, \tag{28}$$

where $E(k)$ is the spectral density of pulsations,

$$E(k) = \int_{|\mathbf{k}|=k} \left|\hat{f}(\mathbf{k})\right|^2 \mathrm{d}\mathbf{k}\,. \tag{29}$$

Relation (28) shows that the wavelet spectrum is always a smoothed version of the Fourier spectrum.

When discussing the properties of multiscale fields, spectra are often used together with structure functions

$$S_q(l) = \left\langle \left(f(\mathbf{x}) - f(\mathbf{x} - \mathbf{l}) \right)^q \right\rangle_{|\mathbf{l}|=l}\,, \tag{30}$$

where angle brackets $\langle \ldots \rangle$ imply averaging over space. In this case, spectral density corresponds to the second-order structure function S_2. Note that if the second-order structure function follows the power law

$$S_2(l) \sim l^{\lambda}\,, \tag{31}$$

the power spectral density

$$E(k) \sim k^{-(\lambda+1)}\,, \tag{32}$$

and the exponent of the wavelet spectrum depends on the parameter κ in definition (24). At $\kappa = 2$, the same power law is valid for the $M(\tau)$ spectrum as for the structure function:

$$M(\tau) \sim \tau^{\lambda}\,; \tag{33}$$

in the case of $\kappa = 3/2$, $M(\tau) \sim \tau^{\lambda+1}$, which is convenient if the wavelet spectrum is compared with the Fourier spectrum $E(k)$. To recall, the scale parameter τ has the same meaning (and dimension) as the distance l in the structure function (30).

An important remark is in order as regards the use of wavelets for the identification of power laws in spectra. Any wavelet has its own spectral image, the tails of which themselves can follow a power dependence. Therefore, the decay rate of these tails determines the limiting decay rate of the spectrum that can be detected by a given wavelet.

Even more caution is needed when using structure functions. The calculation of S_2 in accordance with formula (30) can be interpreted as the calculation of wavelet spectrum (27) using a specific (anisotropic) wavelet formed as a difference between two delta functions spaced by a unit distance,

$$\psi(\mathbf{x}, \mathbf{e}) = \delta(\mathbf{x}) - \delta(\mathbf{x} - \mathbf{e}) , \tag{34}$$

where **e** is the unit vector. This is a very 'bad' wavelet because, having an excellent localization in the physical space, it inevitably has a very poor spectral resolution. This means that structure functions provide very poor scale resolution and can only be used when there is confidence in the smooth behavior of spectral density. In other words, if there is a field, the spectrum of which is a collection of several peaks, the structural functions can transform these peaks into a smoothly decreasing dependence.

The conclusions drawn are illustrated by Fig. 24 showing spectral characteristics of the polarized radio emission map of the same galaxy NGC6946 (the structure function, two wavelet spectra, and the Fourier spectrum). It can be seen that the smooth shape of the graph of the structure function (upper curve) really loses all information about the dominant scales (in this case, they are scales on the order of $0.5'$–$1'$ corresponding to the arm width). An optimal result seems to be the wavelet spectrum obtained using the PH function (second curve from the bottom) that is free of numerous details inherent in the Fourier spectrum but perfectly well identifies the maximum in the energy spectrum.

Figure 24 is borrowed from Ref. [80] in which images of the galaxy NGC6946 obtained in nine different ranges of radio and optical emission were analyzed. Of great interest is the relationship between different types of radio emission; to analyze them in this work, the wavelet cross-correlation function was calculated for each pair of images:

$$r_w(\tau) = \frac{\int w_1(\tau, \mathbf{x}) w_2^*(\tau, \mathbf{x})\, \mathrm{d}\mathbf{x}}{\left(M_1(\tau) M_2(\tau)\right)^{1/2}} . \tag{35}$$

The quantity r_w being a statistical characteristic, the uncertainty of its estimate $\Delta r_w(\tau)$ is due to the number of independent points n used in its calculation (it depends on the scale and is taken equal to $n = (L/\tau)^2$) and to the correlation level itself [81]:

$$\Delta r = \sqrt{\frac{1 - r^2}{n - 2}} . \tag{36}$$

Figure 24b illustrates the wavelet correlation for the pairs of distributions of hydrogen, polarized radio emission, and thermal radiation. It demonstrates how different these three dependences are. The lower curve presents significant

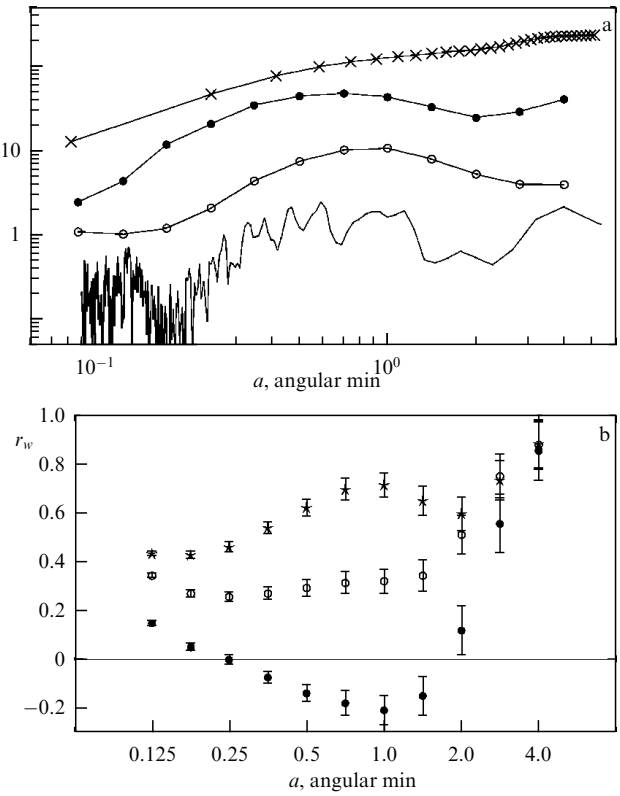

Figure 24. Spectral characteristics of image of the galaxy NGC6946: structure function, wavelet spectra with two different analyzing wavelets, and the Fourier spectrum (top to bottom in Fig. a); wavelet cross-correlation between three pairs of images (b): hydrogen-polarized radio emission (black dots), hydrogen-thermal radiation (asterisks), hydrogen-non-thermal radiation (circles). (From [80].)

negative values on scales comparable to the width of galactic arms, showing that polarized radio emission (an indicator of the presence of magnetic fields) is stronger outside gas arms. The figure also indicates errors in determining the r_w value. The errors increase on large scales due to a reduction in the number of independent points used in the calculation of the correlation coefficient.

Such a large-scale cross-correlation analysis was applied to processing radio images of the M31 and M33 galaxies [82] as well as the M83 galaxy [83].

4.2 Anisotropic analysis

It seems attractive to analyze the structure of spiral galaxies using *anisotropic* wavelets, i.e., families of functions that have a third characteristic (orientation) in addition to scale and position. The simplest real anisotropic wavelet can be constructed using the aforementioned 'Mexican hat' and keeping the power-law dependence only in one coordinate when moving to the plane. This yields the function $\psi(x, y) = (1 - y^2) \exp\left[-(x^2 + y^2)/2\right]$ called the 'Texas hat' in [84] to emphasize its difference from the axisymmetric 'Mexican hat'.

When an anisotropic analyzing function is used for this purpose, the wavelet transform of the two-dimensional field $f(\mathbf{x})$, $\mathbf{x} = (x, y)$ has the form

$$w(\tau, \varphi, \mathbf{x}') = \frac{1}{\tau^{\kappa}} \int_{-\infty}^{+\infty} \int_{-\infty}^{+\infty} f(\mathbf{x}) \psi_{\varphi}\left(\frac{\mathbf{x} - \mathbf{x}'}{\tau}\right) \mathrm{d}\mathbf{x} , \tag{37}$$

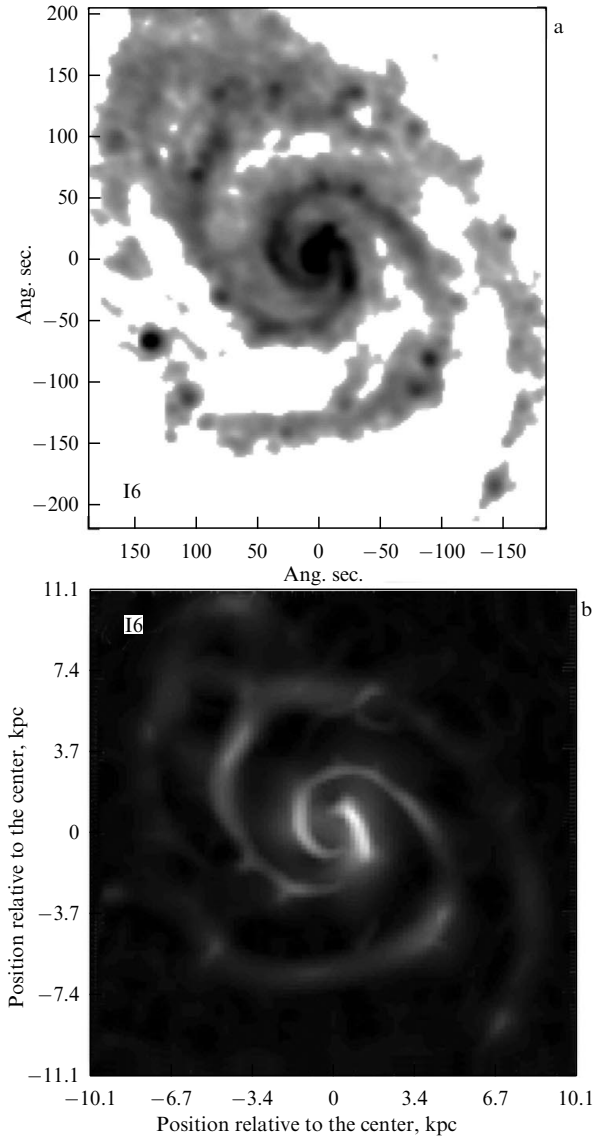

Figure 25. Map of synchrotron radio emission from the M51 galaxy at a wavelength of 6 cm (a) and the result of wavelet-based identification of arms (b). (From [84].)

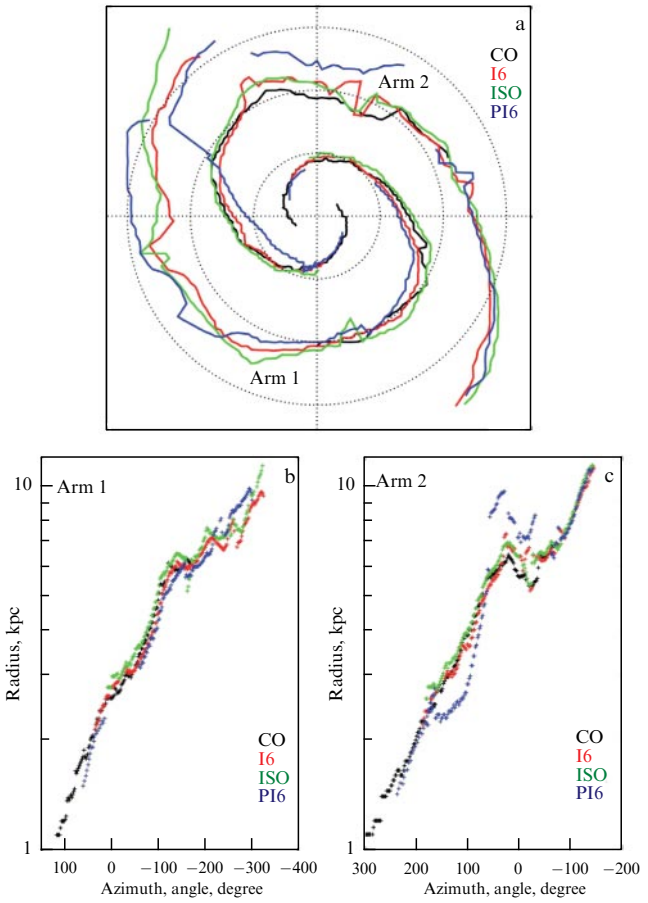

Figure 26. (Color online.) Arms of the M51 galaxy extracted from various radio emission maps (a) and analysis of each arm in terms of the hypothesis of logarithmic arms (b, c). (From [84].)

where the wavelet orientation is given by angle φ, while other notations remain unaltered.

For a given position $\mathbf{x}'$ and a given scale τ, the maximum value of $w(\tau, \varphi, \mathbf{x}')$ over all angles φ,

$$w_{\mathrm{m}}(\tau, \mathbf{x}') = \max_{0 \leqslant \varphi \leqslant \pi} w(\tau, \varphi, \mathbf{x}'), \tag{38}$$

can serve to distinguish the predominant direction defined by the angle φ_{m}, such that $w_{\mathrm{m}}(\tau, \mathbf{x}') = w(\tau, \varphi_{\mathrm{m}}, \mathbf{x}')$.

The distribution of the pulsation energy of the analyzed quantity over the *scales* τ and *orientation directions* φ is determined by the anisotropic wavelet spectrum

$$M(\tau, \varphi) = \int_{-\infty}^{+\infty} \int_{-\infty}^{+\infty} \left| w(\tau, \varphi, \mathbf{x}') \right|^2 \mathrm{d}\mathbf{x}'. \tag{39}$$

Anisotropic wavelets were first used to quantitatively identify arms of the spiral galaxy M51 [84]. Figure 25 shows an example of the identification of spiral arms on the radio emission map of this galaxy; in Fig. 26, arms (more precisely, their 'ridges') extracted from different maps are represented by colored lines on the galactic plane. These constructions allowed the authors to reveal a systematic shift (up to several kiloparsecs) of gas arms and arms visible in radio emission. The presentation of these data in logarithmic coordinates (Fig. 26b, c) made it possible to trace changes in the pitch-angle along the spiral and directly see deviations from the logarithmic spiral. It was shown that two main magnetic arms (identified from polarized radio emission) behave differently: the first quite accurately follows the gas arm (identified from the intensity of CO radiation), with the magnetic field directed along the arm, while the second is markedly shifted relative to the gas arm, and the direction of the magnetic field in it does not coincide with the arm direction [84].

Another relatively nearby galaxy with a pronounced spiral structure, the M83 galaxy, was studied in [83]. This galaxy is a so-called barred galaxy. The bar in the core and the two main arms connected to it are schematically shown in Fig. 27 against the background of emission of cold interstellar gas. The structure of M83 is more complicated than that of M51 as confirmed by the large-scale analysis of radiation maps. The same figure shows results of wavelet filtering using the 'Texas hat' wavelet for two scales, $\tau = 0.35'$ and $\tau = 0.7'$, with the plotted directions of orientation of the dominant structure (angle φ_{m}). Clearly, not only the general pattern of the spiral structure but also the orientation of its elements differs on the presented scales.

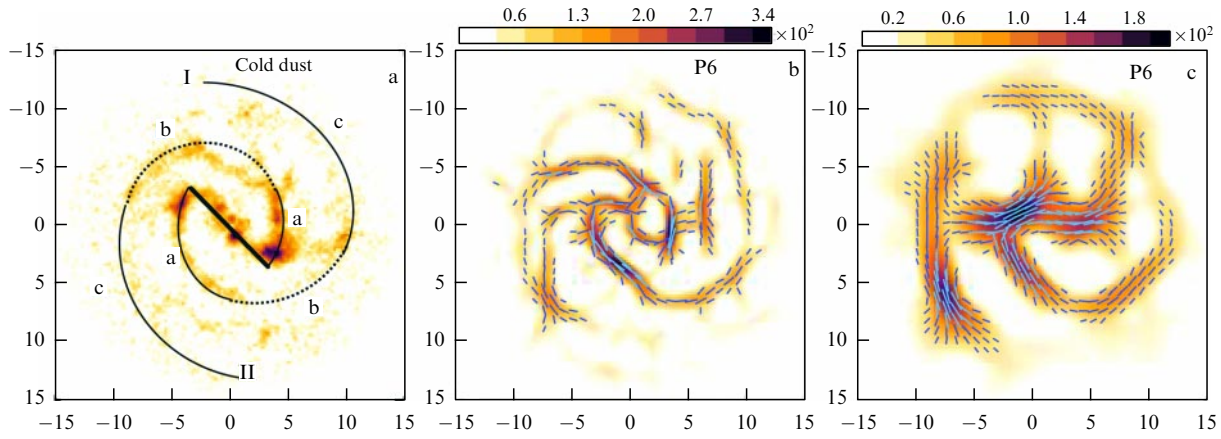

Figure 27. (Color online.) Diagram of bar and two spirals of the M83 galaxy against the background of a cold interstellar gas emission map (a) and results of wavelet filtering of the polarized radio emission map on the scale $\tau = 0.35'$ (b) and $\tau = 0.7'$ (c). Blue lines indicate orientation of the dominant structure (angle φ_m). Galactic coordinates are plotted in kiloparsecs. (From [83].)

One important conclusion ensuing from the analysis performed deserves particular attention. It concerns the absence of regularities in the mutual arrangement (and interaction) of magnetic and gas structures uniform for the entire galaxy. One magnetic arm is displaced relative to the gas arm, just as in the galaxy NGC6946, while the other magnetic arm covers the gas arm, as in the M51 galaxy. This inference is illustrated by Fig. 28 showing directions of magnetic field lines and orientations of anisotropic structures on the arm scale against the background of the gas arm contour (dashed line is the isoline of 20% of the maximum radiation intensity). The left arm (outer part of arm II in Fig. 27) is characterized by a stable correlation of the two directions absent in the other arm and the bar.

Based on the anisotropic wavelet transform, it is possible to introduce the isotropic and anisotropic components through the amplitude of the azimuthal modes $n = 0$ and $n = 2$ (the $n = 1$ mode is equal to zero due symmetry $w(\tau, \varphi, \mathbf{x}) = w^*(\tau, \varphi + \pi, \mathbf{x})$):

$$m^{\mathrm{i}}(\tau, \mathbf{x}) = (2\pi)^{-1} \int_{-\pi}^{+\pi} \left| w(\tau, \varphi, \mathbf{x}) \right|^2 \mathrm{d}\varphi \,, \tag{40}$$

$$m^{\mathrm{a}}(\tau, \mathbf{x}) = (2\pi)^{-1} \int_{-\pi}^{+\pi} \left| w(\tau, \varphi, \mathbf{x}) \right|^2 \exp(2\mathrm{i}\varphi)\, \mathrm{d}\varphi \,, \tag{41}$$

and the corresponding spectra

$$M^{\mathrm{i}}(\tau) = \int_{-\infty}^{+\infty} \int_{-\infty}^{+\infty} m^{\mathrm{i}}(\tau, \mathbf{x}')\, \mathrm{d}\mathbf{x}' \,, \tag{42}$$

$$M^{\mathrm{a}}(\tau) = \int_{-\infty}^{+\infty} \int_{-\infty}^{+\infty} \left| m^{\mathrm{a}}(\tau, \mathbf{x}') \right| \mathrm{d}\mathbf{x}' \,. \tag{43}$$

Furthermore, it is natural to introduce the degree of anisotropy as

$$d_{\mathrm{loc}}^{w}(\tau) = \frac{M^{\mathrm{a}}(\tau)}{M^{\mathrm{i}}(\tau)} \,. \tag{44}$$

The degree of global anisotropy can be calculated through averaging over the complex wavelet coefficients $m^{\mathrm{a}}(\tau, \mathbf{x})$ instead of their amplitudes, so that different phases compensate each other:

$$d_{\mathrm{glob}}^{w}(\tau) = \frac{\left| \int_{-\infty}^{+\infty} \int_{-\infty}^{+\infty} m^{\mathrm{a}}(\tau, \mathbf{x})\, \mathrm{d}\mathbf{x} \right|}{M^{\mathrm{i}}(\tau)} \,. \tag{45}$$

Figure 29 presents a demo in which the test distribution of anisotropic structures of the same size but with different aspect ratios and different orientations is considered. A comparison of the local and global degrees of anisotropy makes it possible to estimate the sensitivity of the method. Global anisotropy is provided by structures with an aspect ratio of 3:1 and appears only at scales from 30 to 60 pixels. On smaller scales, local anisotropy dominates due to structures with the 9:1 aspect ratio. The distribution of the degree of anisotropy by scales and angles (Fig. 29c) shows the values of the position angles over which the anisotropic structures are distributed. A wide range of test configurations was considered in [85], where the method was used to analyze the filamentous small-scale structure of molecular clouds in the constellation Aquila and in the polar region (Polaris Flare). In particular, it was shown that, in the Aquila cloud, where active star formation takes place, anisotropic structures of a selected scale having a common orientation dominate. In a calm cloud like the Polaris Flare, anisotropy is predominantly local in nature and is present to the same extent on all scales.

5. Wavelets in experimental physics

Wavelet transforms of one-dimensional signals obtained in various physical experiments give information expanded in the time-frequency space. For example, in MHD flows excited by complex alternating fields, wavelets made it possible to effectively filter out turbulent fluctuations from fluctuations of external electromagnetic fields [86]. Wavelet cross-correlations have been successfully applied to analyze the behavior of large-scale circulation based on data from laboratory and numerical experiments on turbulent convection in closed volumes [87, 88]. In a number of studies, wavelets have been used to study unsteady turbulent flows [89–91].

In this section, three examples of wavelet-based processing of physical measurement data are considered. One

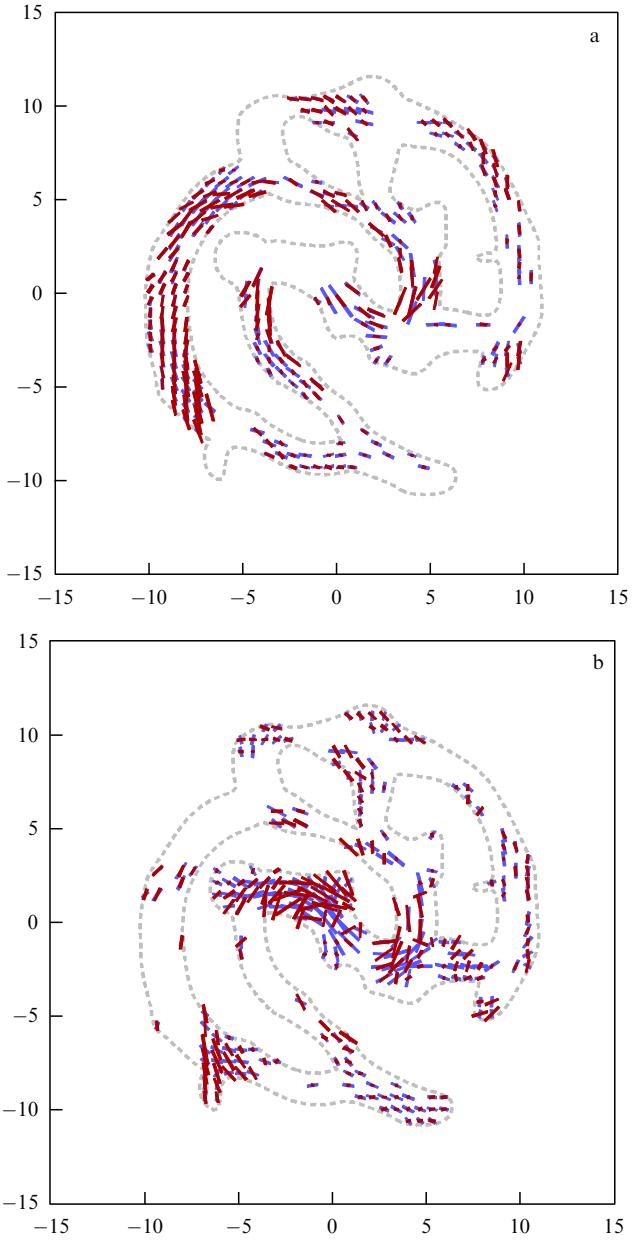

Figure 28. (Color online.) Galaxy M83: direction of the magnetic field (red lines) and of the orientation of gas structures (blue lines) against the background of the gas arm contour (dashed line). Fig. a shows the areas in which both directions are close (less than 33°), Fig. b, the rest of the areas. (From [83].)

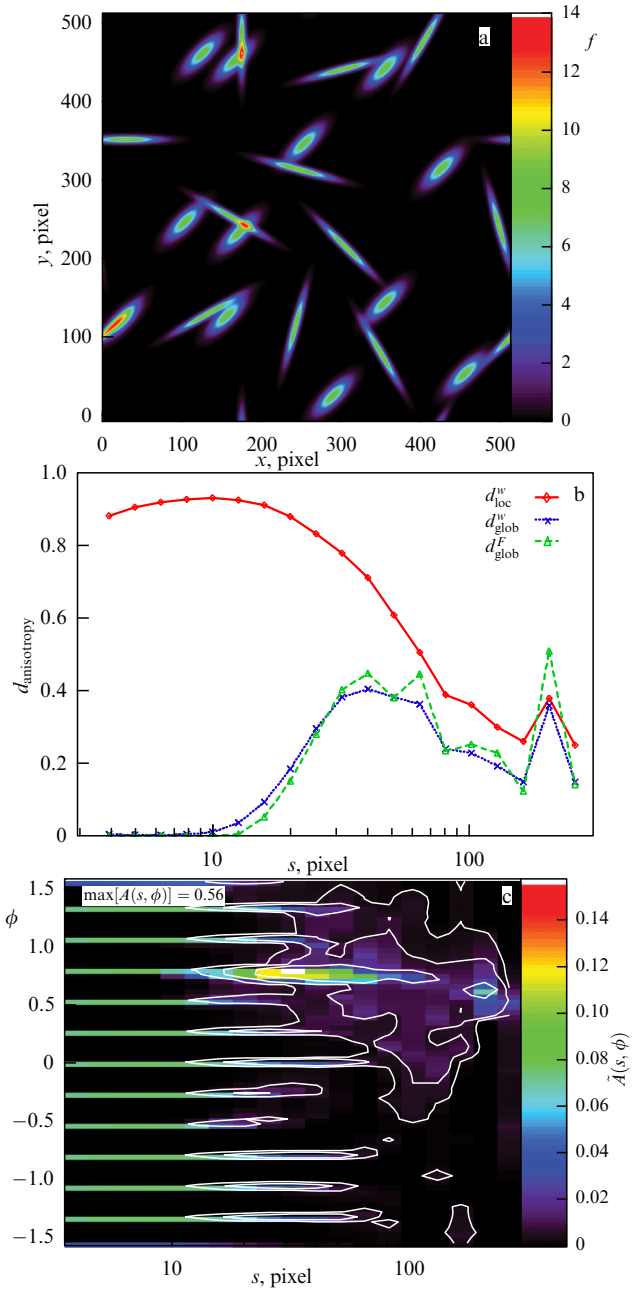

Figure 29. (Color online.) Test distribution of anisotropic structures of two types: all structures with an aspect ratio of 3:1 are oriented at an angle of 45 degrees, and structures with an aspect ratio of 9:1 are oriented randomly. Original image (s). Isotropic and anisotropic spectra (b). Distribution of the degree of anisotropy by scales and angles (c). (From [85].)

concerns an analysis of spectral characteristics of an unsteady flow, the second is related to the processing of signals from multichannel polarization radio telescopes in which wavelets help to solve a nontrivial inverse problem using *a priori* information about the symmetry of the objects of observation, and the third illustrates the use of wavelets to process and analyze signals of a biophysical nature.

5.1 Evolution of spectral characteristics of a pulsed turbulent flow

Let us consider, by way of example of the analysis of unsteady signals, some results of a study on pulsed turbulent flow in a closed channel [92]. This work was done in the context of investigations into the consequences of the generation of magnetic fields by flows of a conducting liquid (see review [47]). These effects become noticeable only at very high Reynolds numbers. More precisely, the governing parameter is the magnetic Reynolds number Rm associated with the usual (hydrodynamic) Reynolds number Re through the magnetic Prandtl number: $\mathrm{Rm} = \mathrm{Re}\,\mathrm{Pm}$. Effects of the generation of magnetic field fluctuations by a turbulent flow manifest themselves at $\mathrm{Rm} \approx 1$, but the problem is the magnetic Prandtl number (the ratio of kinematic viscosity to the diffusion coefficient of the magnetic field) is very small for liquid metals ($\mathrm{Pm} \approx 10^{-5}$), whereas it is necessary to achieve the required magnetic Reynolds numbers with $\mathrm{Re} \approx 10^5$ to generate a liquid metal flow. Therefore, the idea was expressed to create a short

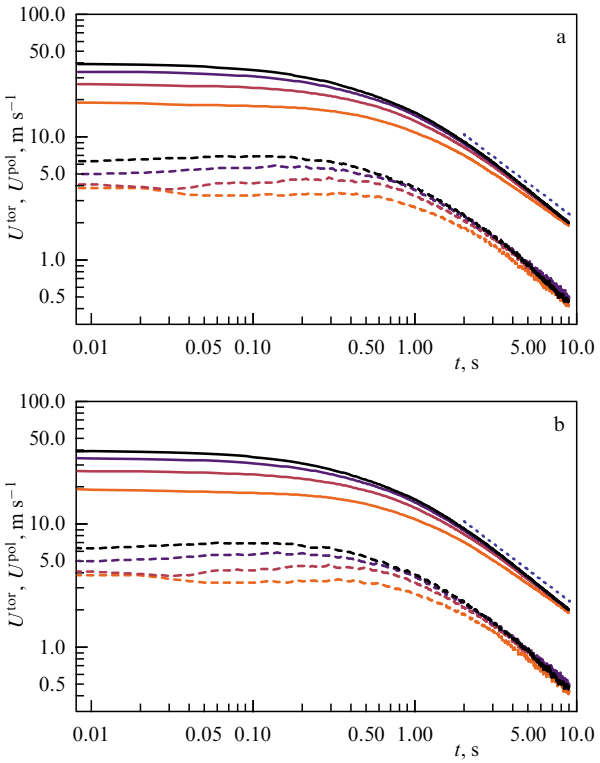

Figure 30. (Color online.) Decay of mean velocity (a) and of rms velocity fluctuations (b) in the pulsed flow of liquid sodium for different channel rotation speeds ($\Omega = 20, 30, 40, 50$ rpm s^{-1}; the lower the speed, the lighter the line). Solid and dashed lines show toroidal and poloidal velocities, respectively. Time is counted from the moment of complete stop of the channel. Dotted line corresponds to the t^{-1} law. (From [92].)

pulsed flow with the required parameters in a toroidal channel filled with liquid sodium [93–95]. In the described experiments, a channel with a radius of 0.18 m and a cross-sectional radius of 0.08 m was used that was first spun up to a speed of 50 revolutions per second and then braked for 0.3 s.

A potential velocity sensor installed in the channel wall made it possible to register both toroidal (along the channel) and poloidal (along the wall but across the channel) velocity components. The picture of evolution of the average values of the two velocity components and the rms values of velocity pulsations is illustrated in Fig. 30 (note that the graphs are given in the double logarithmic coordinates). It can be seen that by the end of braking the toroidal and poloidal velocities reached 40 m s^{-1} and 7 m s^{-1}, respectively, but velocity pulsations dominated in the poloidal component. The evolution of the flow was rapid, with half of the kinetic energy dissipating within the first second after the end of braking. At $t > 1$, velocity pulsations decreased according to the law $\sim t^{-1}$ characteristic of turbulent decay. It is necessary to find out how quickly the inertial interval is formed (whether turbulence has time to develop).

Any stationarity is out of the question in such a case, and wavelets come to the rescue. A spectrogram of the poloidal velocity component obtained using a Morlet wavelet is presented in Fig. 31. It can be seen that, after the termination of braking, a burst of high-frequency pulsations occurs with a peak at frequencies of $\sim 2-4$ kHz. The spot noticeably weakens by the end of the first second, and the frequency at which pulsation energy density reaches a peak decreases.

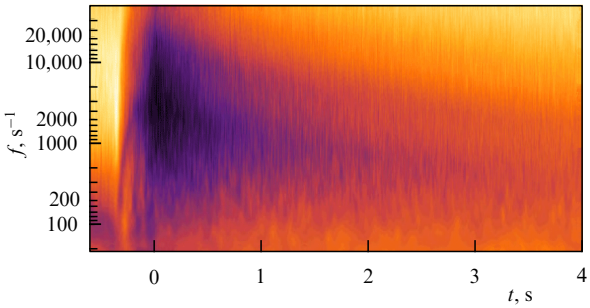

Figure 31. (Color online.) Spectrogram of the velocity poloidal component obtained using a Morlet wavelet for channel rotation speed $\Omega =$ 50 rpm s^{-1}. (From [92].)

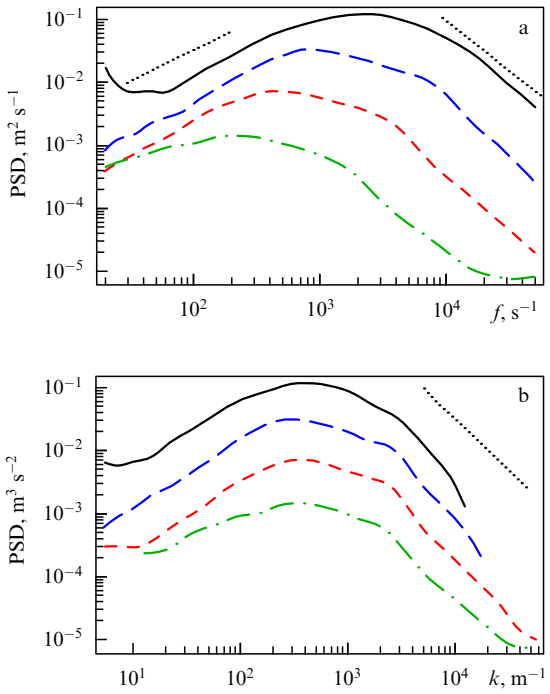

Figure 32. Spectral energy densities of velocity pulsations: (a) time spectra obtained as vertical sections of a wavelet spectrogram (see Fig. 31) averaged over intervals between time instants $t = 0$, 0.5, 1.5, 3.5, 7.5 s (from top to bottom); (b) corresponding spatial spectra recalculated according to the Taylor hypothesis from the mean toroidal flow velocity for each moment. Dotted line shows Kolmogorov's $-5/3$ law for the inertial interval and dependence $E(\omega) \sim \omega$ for the low-frequency part of the spectrum. (From [92].)

Vertical sections of the wavelet spectrogram give instantaneous (or averaged over a reasonable time interval) spectra of velocity pulsations. Figure 32 shows the temporal (frequency) spectra of velocity pulsations, constructed by averaging over four successive time intervals, confirming both the decay of the pulsation energy and the shift of the peak towards low frequencies. The same figure presents the spatial energy spectra of velocity pulsations for the same time intervals. They are obtained by recalculating time frequencies into wavenumbers according to Taylor's hypothesis, taking account of the varying average flow velocity. In the spatial spectra, the energy maximum remains at the same scale determined by the channel diameter. The spatial spectra can be used to get an idea about the stages of formation of the inertial interval.

5.2 RM-synthesis of polarized radio emission of the interstellar medium

The development of observational techniques often leads to such problems with data processing that simply did not occur to specialists of preceding generations and presently require complex and new approaches to data processing. Here is an example of such methods used to explore magnetic fields in galaxies and other celestial bodies on a galactic scale. To recall, the magnetic fields of galaxies are studied by making use of the Faraday effect, the quantitative measure of which is the *Rotation measure* (RM), which requires observations at many wavelengths to be calculated. Until the end of the last century, the word 'many' in this context meant two, three, four or at most six, the usual set of wavelengths being 3, 6, 18, 20 cm, or sometimes another 13 cm. With the advent of broadband radio receivers, it became possible to make observations with a quasi-continuous set of frequencies; at present, observations in many cases are carried out at longer wavelengths, say, in the meter or even decameter range. In the latter case, the plane of polarization can undergo many turns during the propagation of synchrotron radiation through the magnetized medium, while the angle in expression (23) is naturally determined only up to the addition of integer π. The amount of data that can, in principle, be obtained in this way is so large that it turns out to be unrealistic to first carry out observations, e.g., of a nearby outer galaxy at all possible frequencies, then break up the image of the galaxy into small sectors and compare the distribution of polarization angles over sectors and frequencies to plot the magnetic field distribution in this galaxy. Researchers did something like this at the end of the 20th century (see, for example, [96]). Even with observations at three or four wavelengths, the path from data collection to plotting the magnetic field distribution took several years.

It remains to be seen how modern radio astronomy will solve the problem. One of the current approaches is called RM-synthesis. It implies postponing until later the clarification of magnetic field geometry in order to first obtain at least the magnitude of magnetic fields (Faraday rotations, to be precise) of various layers of the magnetized medium through which radiation propagates from the place of emission to the observation point. In many cases, there are several such layers, and the results of RM-synthesis seem to be sufficient to solve the problems really faced by researchers.

The main idea of RM-synthesis [97] has been known for a long time. The classical work [98] held that the degree of polarization of synchrotron radiation $P(\lambda)$ can be considered a Fourier transform in magnitude λ^2 of function F (called Faraday dispersion, which can be used to calculate RM),

$$P(\lambda^2) = \int_{-\infty}^{\infty} F(\phi) \exp(2i\phi\lambda^2)\, d\phi\,. \tag{46}$$

Here, the quantity ϕ is the Faraday depth defined as

$$\phi(z) = -0.81 \int_z^0 B_{||} n_e\, dz'\,, \tag{47}$$

where $B_{||}$ is the component of the magnetic field along the beam, n_e is the density of thermal electrons, and the integral is taken from the source to the observer ($z = 0$).

If observations were made in a wide range of wavelengths λ, it would be necessary to take the inverse Fourier transform in the variable λ^2 from the degree of polarization and receive the desired answer. The only problem is that λ^2 is an essentially positive quantity and must change from $-\infty$ to $+\infty$ in the inverse Fourier transform. Moreover, it is practically impossible to cover the entire range of the required integration in the region of positive λ^2. Additional information is needed to resolve the issue. Therefore, for an isolated object, the problem of negative λ^2 can be solved by taking account of its symmetry. However, even if there are two objects in the path of radiation, the problem cannot be solved by Fourier analysis methods. Wavelet analysis, which allows the Fourier transform to be performed locally, also contributes to the solution to these problems, making it possible to apply the properties of symmetry for each isolated object in the space of Faraday depths [99–101].

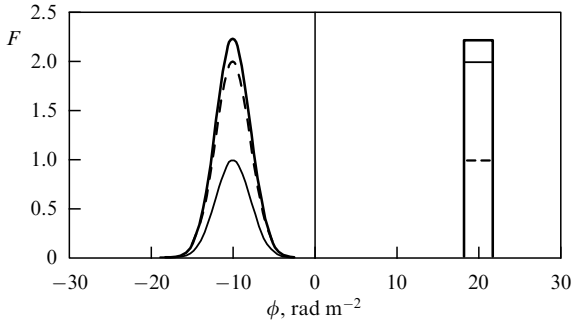

Figure 33. Test example of Faraday dispersion used for RM-synthesis: thick solid line indicates the Faraday dispersion modulus; thin solid line, the real part; dashed line, the imaginary part. (From [99].)

To demonstrate the efficiency of the RM-synthesis idea, a test signal with two localized sources needs to be considered, one characterized by the smooth magnetic field distribution modeled by Gaussians and the other showing a box-like distribution with sharp boundaries (Fig. 33). In both cases, the distribution of Faraday dispersion is symmetric with respect to the middle of the source. This distribution corresponds to the quadrupole symmetry of the galactic magnetic field. Let us calculate complex polarization corresponding to a given Faraday dispersion. Of course, it is defined only for positive λ^2 but can be formally extended to the region of negative λ^2 using the properties of quadrupole symmetry of the Faraday dispersion. Now, it is possible to calculate wavelet coefficients of complex polarization (their distribution on the wavelet plane is shown in Fig. 34a) and to restore the original signal using the inverse wavelet transform (Fig. 34b). It can be seen that the reconstructed signal is indeed similar to the original one.

Naturally, when analyzing the data obtained with a real radio telescope that receives signals only within a limited wavelength range only part of the information about the original Faraday dispersion is restored. A wavelet analysis helps us to understand what part of the information can be obtained in this way. Let us consider, as an example, the potential of a radio telescope operating at long waves ($0.6 < \lambda < 0.78$ m (Fig. 34b, c) and $0.6 < \lambda < 2.5$ m (Fig. 34e, f)). These examples illustrate difficulties encountered in observations confined to long wavelengths and to a certain extent simulate the efficiency of the LOw Frequency ARray (LOFAR) telescope. It can be seen that information about the first source is almost completely lost in both wavebands. In the first of the ranges, it is possible to restore the localization of the second source, and the expansion of the range to the long-wave region makes it possible to fix the position of the boundaries of the second source. It can be

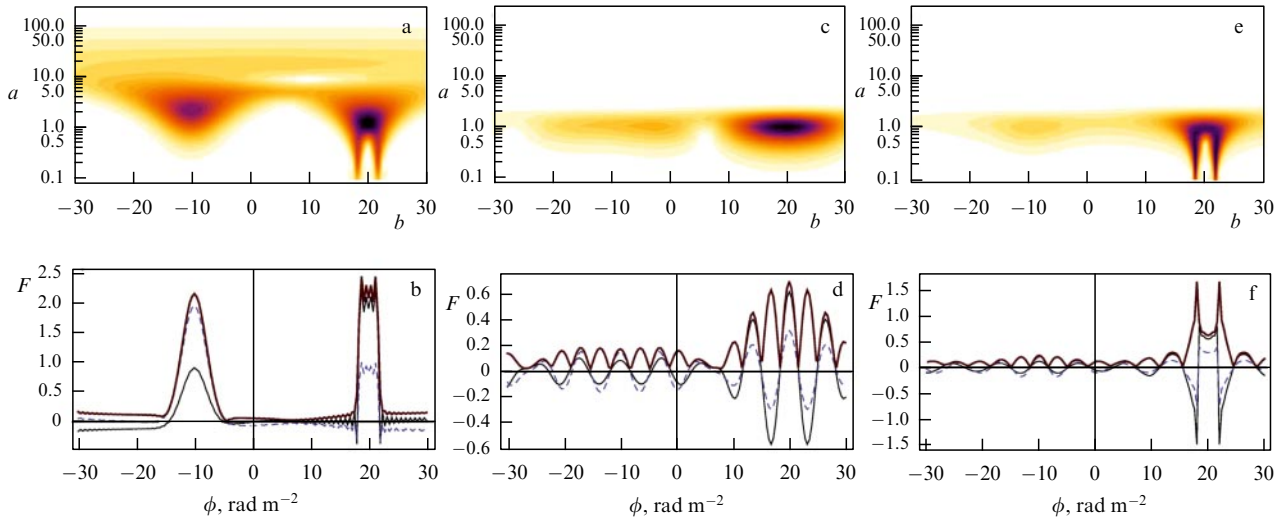

Figure 34. (Color online.) RM-synthesis using wavelets for the signal from Fig. 33. Wavelet spectrograms (a, c, e) and results of reconstruction for the entire wavelength range (b), for $0.6 < \lambda < 0.78$ m (d), and for $0.6 < \lambda < 2.5$ m (e). Corresponding reconstruction of F (b, d, f): thin solid line indicates the real part; dashed line, the imaginary part; solid bold line, the modulus. (From [99].)

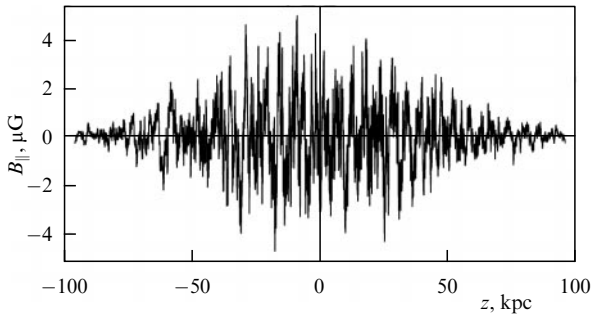

Figure 35. Test example of a small-scale magnetic field. (From [101].)

verified whether the inclusion of an area up to $\lambda = 0.03$ m into the measurement range makes it possible to reconstruct the Faraday dispersion almost as completely as in Fig. 34a, b. This wavelength range corresponds to characteristics of the Square Kilometer Array (SKA) telescope under construction, which demonstrates the advantages of this instrument for observing the magnetic fields of spiral galaxies. It should be emphasized that each telescope has specific limitations making it more suited for one set of tasks and less so for another.

The above example shows that observations of long waves that are presently very popular due to the advent of the new-generation LOFAR telescope first of all contain information about regions with abrupt changes in the magnetic field. This conclusion can be confirmed by another test example (Fig. 35), in which the magnetic field is localized within a certain extended layer and has a pronounced small-scale turbulent structure. We have analyzed the corresponding signal in the wavelength ranges typical of operating radio telescopes and those currently under construction (Fig. 36). Evidently, observations with the SKA telescope will allow transmitting all the main details of the signal, whereas observations in a narrow range of long waves (with the Westerbork Synthesis Radio Telescope (WSRT) with two narrow wavebands) give information only on the general localization of a small-scale signal, and the expansion of the range towards long waves (characteristic of LOFAR) allows conveying small-scale signal details. To date, a version of RM-synthesis based on the use of wavelets has undergone comprehensive testing and a comparison with other algorithms and has demonstrated advantages inherent in wavelets [102].

Based on the discussed characteristics of wavelets, the following steps can be taken to use observations of long waves to explore the magnetic fields of galaxies. It is known from studies involving a small set of wavelengths that the magnetic fields in spiral galaxies form rather narrow spiral arms that can be shifted relative to the spiral arms in the distribution of

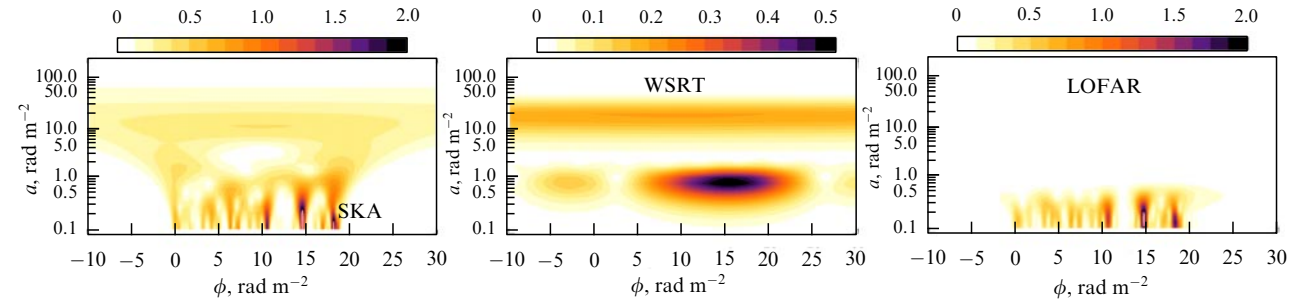

Figure 36. (Color online.) Wavelet spectrograms of a model turbulent signal (see Fig. 35) 'visible' in the wavelength ranges of three radio telescopes: (a) $\lambda \in [0.03; 4.3]$ (SKA), (b) $\lambda \in [0.17; 0.23] \cup [0.77; 0.97]$ (WSRT), and (c) $\lambda \in [1.25; 2.73]$ (LOFAR). (From [101].)

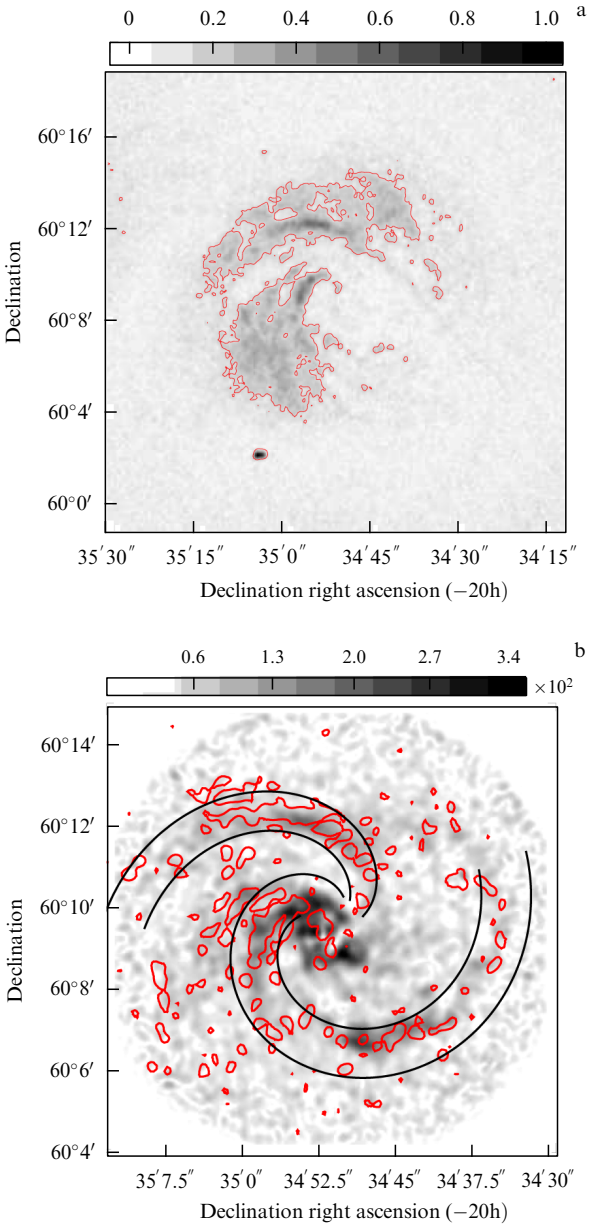

Figure 37. Identification of magnetic spiral arms in the galaxy NGC 6946 from observations in the range of 0.17–0.23 m: (a) standard RM-synthesis, (b) analysis using wavelets. (From [71].)

interstellar gas and stars [103]. In multichannel observations within a relatively narrow wavelength range (0.17–0.23 m), RM-synthesis making no use of wavelets reveals only two diffuse spots at the place of two narrow magnetic arms (Fig. 37) due, in particular, to the fact that, the more channels there are, the shorter the observation time of each of them; as a result, the signal-to-noise ratio deteriorates. Of course, one can integrate the signal over the spectrum and restore the ratio of the signal to noise characteristic of single-channel observations, but that would be akin to emulating the operation of a previous-generation telescope on a modern one. Certainly, one could wait for the commissioning of the SKA telescope expected to enable researchers to take advantage of short-wavelength observations, but they seek to have results as soon as possible. The wavelet analysis allows estimating the contribution of small-scale magnetic fields, to which the telescope is most sensitive.

Wavelet RM synthesis was generalized to a two-dimensional case and applied to multichannel data on the galaxy NGC 6946 obtained by observations using the LOFAR radio telescope. It was possible to detect the trail of magnetic spiral arms that are not visible by other methods [104]. A wavelet analysis of artificial data confirmed that the discovered effect is underlain by the depolarization mechanism [105].

5.3 Biosignals in medical physics

It seems important to emphasize the universal character of the described methods for recording, treating, and analyzing signals in the framework of this review. The practical choice of a particular method of analysis is dictated not so much by the nature of the signal as by its structure and by what one expects to clarify as a result of the analysis.

An excellent example of a complex nonlinear system with tangled temporal dynamics is the human body, the existence of which is maintained by two pronounced quasiperiodic processes — the work of the heart and respiration, against the background and under the direct influence of which a whole spectrum of cyclic processes associated with the vital activity of the organism is formed. There are many examples of successful application of wavelets for signal processing in medicine. Suffice it to mention reviews on wavelet analysis of cardiac signals [106] and neurodynamics [13], as well as some work analyzing the dynamics of peripheral blood flow [107–111]. Figure 38 exemplifies the fundamental role of wavelet algorithms in the cross-correlation analysis of temperature pulsations on the skin surface and of the signals from a laser Doppler flowmeter used to evaluate the intensity of the peripheral blood flow in subcutaneous layers. The structures of the two signals in Figs 38a, b are altogether different; however, the module of the wavelet cross-correlation function shown in Fig. 38c demonstrates a high degree of correlation in the frequency range from 0.01 to 0.1 Hz [110]. It is this frequency range that is especially interesting from the standpoint of elucidation of the microcirculation mechanism. The presented graph is equally interesting in terms of the calculation of function (12) using wavelet (2) with different values of the parameter σ. The same is true of the results of test calculations for surrogate (random series with similar spectral properties) data confirming the significance of the estimates obtained.

It is worthwhile to mention results of an analysis of a signal from a polyrheocardiograph, a device for recording various characteristics of cardiac activity, as an example of the application of wavelet analysis to the study of time-dependent variability of a system dominated by two quasi-periodic processes [112].

Impedance rheocardiography (ICG) is a simple, inexpensive, noninvasive method for studying the central hemodynamics to be used to determine one of its key indicators — the stroke volume — and to assess cardiac output, total peripheral vascular resistance, time of blood expulsion from the left ventricle, and other parameters. The method is essentially based on the registration of changes in the electrical resistance of biological tissues during the passage of high-frequency alternating current.

An ICG signal has a set of characteristic points and waves designated B, E, X, O in Fig. 39. These points are associated with various physiological events in the cardiac cycle. Point B is synchronized with the first heart sound that occurs when the atrioventricular valves close at the very beginning of the ventricular systole. Sometimes, determining the location of

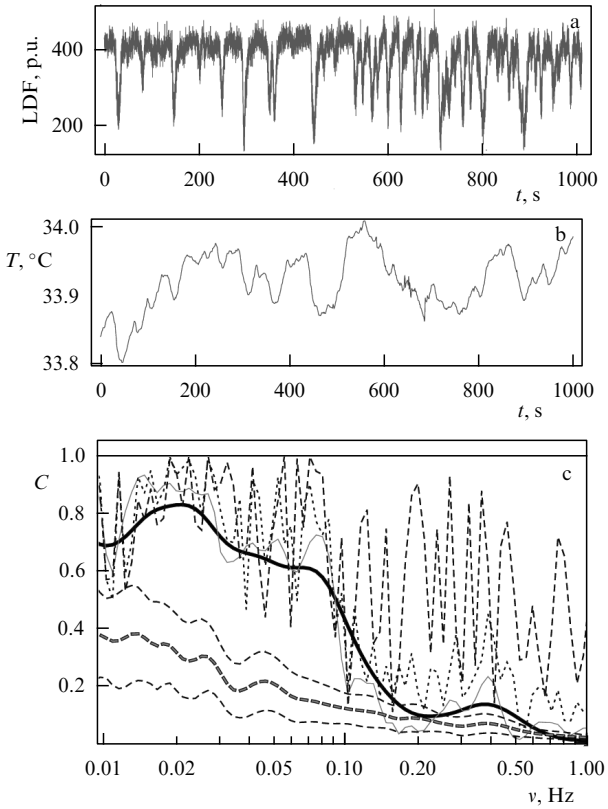

Figure 38. (a) Signal from a Doppler flowmeter characterizing the intensity of blood flow in the tissue (in perfusion units), (b) skin temperature, (c) modulus of the wavelet cross-correlation function for these signals calculated using the Morlet wavelet for $\sigma = 1$ (bold black line), $\sigma = 2$ (thin line), $\sigma = 10$ (dotted line), $\sigma = 100$ (dashed line), $\sigma = \infty$ (thin horizontal line). Bold dashed line shows the result of calculations for 70 realizations of surrogate data. Thin dashed lines represent the first and third quartiles. (From [110].)

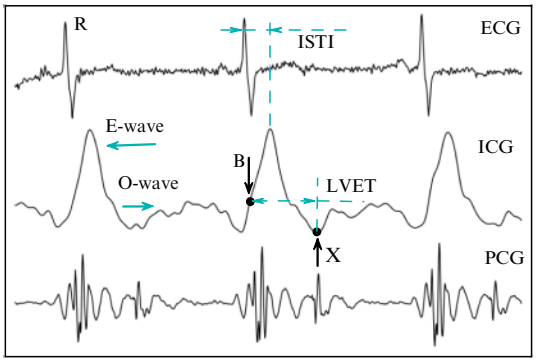

Figure 39. Typical polyrheocardiograph signals: electrocardiogram (ECG), differential rheocardiogram (impedance rheocardiogram, ICG), and phonocardiogram (PCG). (From [106].)

point B is problematic, since the shape of the ICG signal in this area is not always clearly expressed. Point E is the maximum on a differential rheogram. It represents the highest impedance variation rate, which is, in turn, related to the maximum burst rate measured by ultrasonic techniques. Point X corresponds to the slamming of the semilunar valves at the end of the ventricular systole (and the second heart sound). For ICG, the first maximum (i.e., the E-wave) is associated with the systolic phase of the cardiac cycle, and the second maximum, with a lower amplitude (O-wave), relates to the diastolic phase. The amplitude of the E-wave is proportional to the stroke volume, and the amplitude of the O-wave correlates to the change in the volume of the left atrium during the diastolic phase. In some cases, the O-wave amplitude turns out to be an important diagnostic parameter. The stroke volume is believed to be proportional to the ejection time and the maximum value of the first derivative of the impedance dZ/dt for a given cycle. Left ventricular ejection time (LVET) is defined as the time interval between the opening of the aortic valve and its subsequent closure.

Note that wavelets are widely used in the analysis of medical signals, but their use is practically always restricted to filtering performed in terms of a discrete wavelet transform. The prospects for wavelet analysis are much wider: in Refs [112, 113], the apparatus of continuous wavelet transform was used not only to filter the signal of a rheocardiograph but also to regularize the treatment of initial signals, evaluating the degree of correlation between signals in a given frequency band, and determining quantitative functional characteristics of the heart, such as stroke volume. A technique was proposed for the assessment of the functional state of the cardiovascular system based on the analysis of two-dimensional time-frequency distributions of wavelet coefficients for converting differential rheogram curves. It is possible to recognize characteristic features in systolic and diastolic phases of the cardiac cycle in images (wavelet portraits) of cardiocycles in various groups of patients.

Typical wavelet images of differential rheograms and phonocardiograms of three consecutive cardiocycles are shown in Fig. 40. It is highly apparent that each of the three successive cycles has its own 'portrait,' even when a patient is at rest. The extended structures in Fig. 40b correspond to one breathing cycle (inhalation and exhalation).

Traditionally, the stroke volume in ICG is defined as the product of the maximum of the first derivative in the rheogram and the expulsion time, with the corresponding anthropometric coefficients and taking into account the total bioimpedance. In standard methods, the E-wave amplitude is determined after setting the rheogram to the isoline, i.e., after the compensation of respiratory and motor artifacts. The application of the wavelet-based approach allows separating the pulse and respiratory waves and determining the amplitude of the E-wave wavelet coefficients. LVET is inferred from the scale of this wave. This approach ensures a greater accuracy than that provided by the method for determining expulsion time from the characteristic points of a differential rheogram. In the context of this approach, the ISTI parameter is defined as the time interval between the R-peak on the ECG and the maximum of the wavelet representation of the E-wave.

To verify the method, the authors of [112] examined 12 healthy men aged 20 to 25 who made up the control group and 14 patients with a diagnosis of essential hypertension. Polyrheocardiography was used, by which an ECG and phonocardiogram were obtained simultaneously with ICG. During the registration of polyrheocardiograms, an isometric load test was carried out (raising the legs from a horizontal position and holding them at an angle of 30–45 degrees). The healthy patients experienced a linear increase in E- and O-wave amplitudes during the stress test. Following termination of the load (lowering the legs to a horizontal position), the amplitudes of the E- and O-waves took on their initial values. The linear increase in the stroke volume during the exercise corresponded to a normal physiological response.

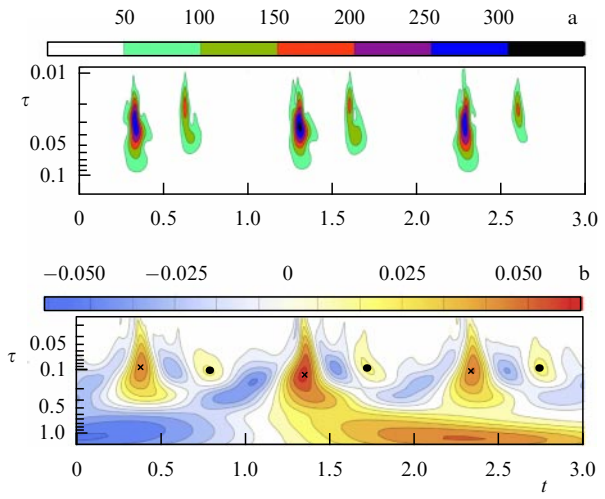

Figure 40. (Color online.) Wavelet images of three cardiocycles based on phonocardiography (a) and impedance rheocardiography (b) signals where E-wave maxima are indicated by crosses, and O-waves, by dots. (From [112].)

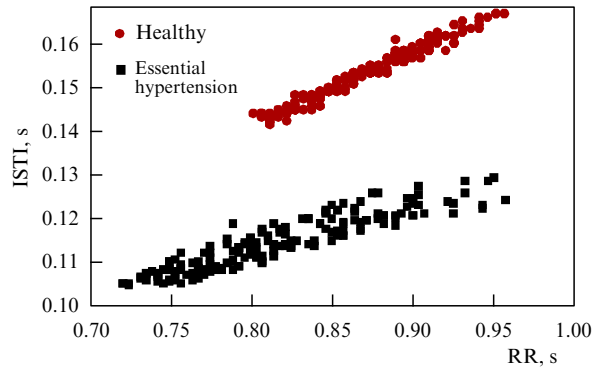

Figure 41. (Color online.) Exercise test: dependence of ISTI interval on RR interval calculated from the results of wavelet analysis for healthy (red dots) and sick (black dots) subjects. (From [112].)

For patients with hypertension, weak changes in the amplitudes of E- and O-waves and a shortening of the ISTI interval during the test were observed, which suggested a serious derangement of compensatory mechanisms. Figure 41 shows the relationship between the lengths of ISTI and RR intervals in healthy and sick patients, indicating that the wavelet method allows these groups to be unambiguously separated.

6. Conclusion

We tried to show in the present review how, in the few decades of its history, wavelet analysis has moved from a mathematical novelty to a familiar toolbox of physicists. The volume of physical literature concerning wavelets is such that its representative citation would reduce this article to a bibliographic list. Therefore, we started with simple and obvious matters and gradually moved on to complex ones. Of course, this strategy is subjective and based primarily on the experience of our group. However, it is clear, even within the framework of such a choice, that applications of wavelets are associated not so much with the traditional areas of laboratory physics as with areas like astronomy, geophysics, and medical physics. Wavelets are also used in laboratory experiments, but here, too, we are talking mostly about new and not quite standard studies, such as nonstationary hydrodynamic and magnetohydrodynamic experiments.

A comparison of the development of wavelet analysis and the Fourier method reveals a similarity. Many branches of modern physics, such as spectral analysis, are simply impossible to imagine outside the context of ideas behind the Fourier method. These areas of physical science, in turn, greatly contributed to the elaboration of basic principles underlying the Fourier method. We believe that a similar development path awaits wavelet analysis. The wavelet representation of the spectral properties of a signal is an extensively developing analytical apparatus for the treatment of post-processing observational, experimental, and mathematical simulation data. Some of its tools were comprehensively tested and have become routine applications in research practice. The new variants of wavelet analysis being constantly proposed not infrequently duplicate one another, and their use necessitates a more attentive attitude to the results and details of interpretation. This, in fact, is the subject matter of the present review.

It follows from the above that, in many areas of physics and related sciences, ideas about cyclic processes constantly arise. The most superficial acquaintance with the experimental and observational material on which such ideas are based suggests that researchers are actually dealing with something different from periodic processes in the literal sense. The set of such situations is rapidly expanding beyond the bounds of traditional physical disciplines.

The gradual development of new boundary regions of physics seems to be a natural tendency within the framework of which wavelet analysis can and should, we think, play a key role. In this sense, it seems remarkable that this review was written within the framework of the RFBR-Expansion program.

This paper was supported by the Russian Foundation for Basic Research (RFBR project 19-11-50217). The authors are grateful to Ilya Usoskin and Leif Svalgaard for advice on data selection when updating results of some papers reviewed in this review.

References

1. Yaglom A M *Korrelyatsionnaya Teoriya Statsionarnykh Sluchainykh Funktsii s Primerami iz Metrologii* (The Correlation Theory of Stationary Random Functions with Examples from Metrology) (Leningrad: Gidrometeoizdat, 1981)
2. Gabor D *J. Inst. Electr. Eng.* **93** 429 (1945)
3. Grossmann A, Morlet J *SIAM J. Math. Anal.* **15** 723 (1984)
4. Meyer Y *Wavelets and Operators* (Cambridge: Cambridge Univ. Press, 1992)
5. Daubechies I *Ten Lectures on Wavelets* (Philadelphia, Pa.: Society for Industrial and Applied Mathematics, 1992)
6. Holschneider M *Wavelets: an Analysis Tool* (New York: Oxford Univ. Press, 1995)
7. Torresani B *Continuous Wavelet Transform* (Paris: Savoire, 1995)
8. Mallat S *A Wavelet Tour of Signal Processing: The Sparse Way* 3rd ed. (Amsterdam: Elsevier. Academic Press, 2009)
9. Farge M *Annu. Rev. Fluid Mech.* **24** 395 (1992)
10. Astaf'eva N M *Phys. Usp.* **39** 1085 (1996); *Usp. Fiz. Nauk* **166** 1145 (1996)
11. Dremin I M, Ivanov O V, Nechitailo V A *Phys. Usp.* **44** 447 (2001); *Usp. Fiz. Nauk* **171** 465 (2001)
12. Pavlov A N, Anishchenko V S *Phys. Usp.* **50** 819 (2007); *Usp. Fiz. Nauk* **177** 859 (2007)
13. Pavlov A N et al. *Phys. Usp.* **55** 845 (2012); *Usp. Fiz. Nauk* **182** 905 (2012)

14. Frick P, Zimin V, in *Wavelets, Fractals and Fourier Transform* (Inst. of Math and its Appl. Conf. Ser. No. 43, Eds M Farge, J Hunt, J Vassilicos) (Oxford: Clarendon Press, 1993) p. 265
15. Frick P et al. *Astron. Astrophys.* **328** 670 (1997)
16. Frick P et al. *Mon. Not. R. Astron. Soc.* **491** 5572 (2020)
17. Bruijn de N G, in *Inequalities*: *Proc. of a Symp., Wright-Patterson Air Force Base* (Ed. O Shisha) (New York: Academic Press, 1965) pp. 57–71
18. Frick P G *Turbulentnost'*: *Podkhody i Modeli* (Turbulence, Methods and Model) 2nd ed. corrected and amended (Moscow–Izhevsk: RKhD, 2010)
19. Tikhonov A N, Arsenin V Ya *Metody Resheniya Nekorrektnykh Zadach* (Methods for Solution of Incorrect Problems) (Moscow: Nauka,1986)
20. Patrikeev I A, Stepanov R A, Frick P G *Vychisl. Metody Programmirovanie* **6** 39 (2005)
21. Bloomfield P *Fourier Analysis of Time Series*: *an Introduction* (New York: Wiley, 1976)
22. Nesme-Ribes E et al. *Comptes Rendus B Acad. Sci. Paris* **321** 525 (1995)
23. Torrence C, Webster P J *J. Climate* **12** 2679 (1999)
24. Guedes M R G, Pereira E S, Cecatto J R *Astron. Astophys.* **573** A64 (2015)
25. Chavez M, Cazelles B *Sci. Rep.* **9** 7389 (2019)
26. Soon W et al. *Earth-Sci. Rev.* **134** 1 (2014)
27. Velasco Herrera V M et al. *New Astron.* **56** 86 (2017)
28. Frick P et al. *Astophys. J.* **483** 426 (1997)
29. Frick P, Grossmann A, Tchamitchian P *J. Math. Phys.* **39** 4091 (1998)
30. Soon W et al. *Mon. Not. R. Aston. Soc.* **483** 2748 (2019)
31. Monin A S *Sov. Phys. Usp.* **23** 594 (1980); *Usp. Fiz. Nauk* **132** 123 (1980)
32. Vitinskii Yu I, Konetskii M, Kuklin G V *Statistika Pyatnoobrazovatel'noi Deyatel'nosti Solntsa* (Statistics of Solar Spot-Forming Activity) (Moscow: Nauka, 1986)
33. Soon W W-H, Yaskell S H *The Maunder Minimum and the Variable Sun-Earth Connection* (River Edge, NJ: World Scientific, 2003)
34. Ogurtsov M G et al. *Solar Phys.* **211** 371 (2002)
35. Sokoloff D *Sun Geosphere* **12** 20 (2017)
36. Zolotova N V, Ponyavin D I *Astrophys. J.* **800** 42 (2015)
37. Usoskin I G et al. *Astron. Astrophys.* **581** A95 (2015)
38. Hoyt D V, Schatten K H *Solar Phys.* **179** 189 (1998)
39. Vaquero J M et al. *Solar Phys.* **291** 3061 (2016)
40. Svalgaard L, Schatten K H *Solar Phys.* **291** 2653 (2016)
41. Chatzistergos T et al. *Astron. Astrophys.* **602** A69 (2017)
42. Svalgaard L, Personal communication (2020); in *Sun-Climate Symp. 2020, Tucson, AZ*; "Three Centuries of Validated Monthly Sunspot Groups Numbers", https://leif.org/research/Three-Centuries-of-Validated-Sunspot-Group-Numbers.pdf
43. Pipin V V, Sokoloff D D, Usoskin I G *Astron. Astrophys.* **542** A26 (2012)
44. Kitchatinov L L, Mordvinov A V, Nepomnyashchikh A A *Astron. Astrophys.* **615** A38 (2018)
45. Bazilevskaya G et al. *Space Sci. Rev.* **186** 359 (2014)
46. Ruzmaikin A *Phys. Usp.* **57** 280 (2014); *Usp. Fiz. Nauk* **184** 297 (2014)
47. Sokoloff D D, Stepanov R A, Frick P G *Phys. Usp.* **57** 292 (2014); *Usp. Fiz. Nauk* **184** 313 (2014)
48. Plunian F, Sarson G R, Stepanov R *Mon. Not. R. Astron. Soc.* **400** L47 (2009)
49. Pipin V V, Kosovichev A G *Astrophys. J.* **867** 145 (2018)
50. Sych R A *Solar-terrestrial Phys.* **1** (2) 3 (2015)
51. Sych R A, Nakariakov V M *Solar Phys.* **248** 395 (2008)
52. Sych R et al. *Astron. Astrophys.* **539** A23 (2012)
53. Sych R et al. *Astron. Astrophys.* **577** A43 (2015)
54. Laclare F *Astron. Astrophys.* **125** 200 (1983)
55. Lanza A F *Proc. Int. Astron. Union* **5** (S264) 120 (2009)
56. Goncharskii A V et al. *Sov. Astron.* **26** 690 (1982); *Astron. Zh.* **59** 1146 (1982)
57. Miyake F, Usoskin I, Poluianov S (Eds) *Extreme Solar Particle Storms* (Bristol: IOP Publ., 2019)
58. Frick P et al. *New Astron.* **9** 599 (2004)
59. Baliunas S et al. *Mon. Not. R. Astron. Soc.* **365** 181 (2006)
60. Baliunas S et al. *Solar Phys.* **224** 179 (2004)
61. Sosnovtseva O V et al. *Phys. Rev. E* **70** 031915 (2004)
62. Sosnovtseva O V et al. *Phys. Rev. Lett.* **94** 218103 (2005)
63. Soon W, Frick P, Baliunas S *Astrophys. J.* **510** L135 (1999)
64. Stepanov R et al. *Mon. Not. R. Astron. Soc.* **495** 3788 (2020)
65. Katsova M M, Bondar N I, Livshits M A *Astron. Rep.* **59** 726 (2015); *Astron. Zh.* **92** 596 (2015)
66. Stefani F et al. *Astron. Nachr.* **341** 600 (2020)
67. Baliunas S et al. *Geophys. Res. Lett.* **24** 1351 (1997)
68. Panovska S, Finlay C C, Hirt A M *Earth Planet. Sci. Lett.* **379** 88 (2013)
69. Galyagin D K et al. *Dokl. Earth Sci.* **360** 617 (1998); *Dokl. Ross. Akad. Nauk* **360** 541 (1998)
70. Sokoloff D D, Shibalova A S *Izv. Phys. Solid Earth* **51** 764 (2015); *Fiz. Zemli* (5) 156 (2015)
71. Sokoloff D D, Shibalova A S *Geomagn. Aeron.* **58** 888 (2018)
72. Gruzdev A N, Bezverkhnii V A *J. Atmos. Solar-Terr. Phys.* **187** 53 (2019)
73. Zhao X H, Feng X S *J. Atmos. Solar-Terr. Phys.* **122** 26 (2015)
74. Burakov K S et al. *Izv. Phys. Solid Earth* **34** 773 (1998); *Izv. Ross. Akad. Nauk. Fiz. Zemli* **34** 83 (1998)
75. Klausner V et al. *J. Atmos. Solar-Terr. Phys.* **92** 124 (2013)
76. Klausner V et al. *J. Geophys. Res. Space Phys.* **119** 3077 (2014)
77. Ginzburg V L *Propagation of Electromagnetic Waves in Plasma* (New York: Gordon and Breach, 1961); Translated from Russian: *Rasprostranenie Elektromagnitnykh Voln v Plazme* (Moscow: Fizmatgiz, 1960)
78. Stepanov R A, Sokoloff D D *Phys. Usp.* **62** 1208 (2019); *Usp. Fiz. Nauk* **189** 1285 (2019)
79. Frick P et al. *Mon. Not. R. Astron. Soc.* **318** 925 (2000)
80. Frick P et al. *Mon. Not. R. Astron. Soc.* **327** 1145 (2001)
81. Edwards A L *Multiple Regression and the Analysis of Variance and Covariance* (San Francisco, CA: W.H. Freeman, 1979)
82. Tabatabaei F S et al. *Astron. Astrophys.* **557** A129 (2013)
83. Frick P et al. *Astron. Astrophys.* **585** A21 (2016)
84. Patrikeev I et al. *Astron. Astrophys.* **458** 441 (2006)
85. Ossenkopf-Okada V, Stepanov R *Astron. Astrophys.* **621** A5 (2019)
86. Kolesnichenko I et al. *Exp. Fluids* **56** 88 (2015)
87. Khalilov R et al. *Phys. Rev. Fluid* **3** 043503 (2018)
88. Vasiliev A et al. *Int. Commun. Heat Mass Transfer* **108** 104319 (2019)
89. Noskov V et al. *Magnetohydrodynamics* **55** 149 (2019)
90. Frick P et al. *Magnetohydrodynamics* **51** 267 (2015)
91. Mikhailovich B, Shapiro A, Stepanov R *Magnetohydrodynamics* **52** 125 (2016)
92. Noskov V et al. *Phys. Rev. E* **85** 016303 (2012)
93. Frick P et al. *Magnetohydrodynamics* **38** 143 (2002)
94. Noskov V et al. *Phys. Fluids* **21** 045108 (2009)
95. Frick P et al. *Phys. Rev. Lett.* **105** 184502 (2010)
96. Ruzmaikin A A, Shukurov A M, Sokoloff D D *Magnetic Fields of Galaxies* (Astrophysics and Space Science Library, Vol. 133) (Dordrecht: Kluwer Acad. Publ., 1988); Ruzmaikin A A, Sokoloff D D, Shukurov A M *Magnitnye Polya Galaktik* (Moscow: Nauka, 1988)
97. Brentjens M A, de Bruyn A G *Astron. Astrophys.* **441** 1217 (2005)
98. Burn B J *Mon. Not. R. Astron. Soc.* **133** 67 (1966)
99. Frick P et al. *Mon. Not. R. Astron. Soc.* **401** L24 (2010)
100. Frick P et al. *Mon. Not. R. Astron. Soc.* **414** 2540 (2011)
101. Beck R et al. *Mon. Not. R. Astron. Soc.* **543** A113 (2012)
102. Sun X H et al. *Astron. J.* **149** 60 (2015)
103. Beck R, Hoernes P *Nature* **379** 47 (1996)
104. Chupin A et al. *Astron. Nachr.* **339** 440 (2018)
105. Sokoloff D et al. *Galaxies* **6** (4) 121 (2018)
106. Stepanov R et al., in *Bioimpedance in Biomedical Applications and Research* (Eds F Simini, P Bertemes-Filho) (Cham: Springer Intern. Publ., 2018) p. 257
107. Podtaev S, Morozov M, Frick P *Cardiovascular Eng.* **8** 185 (2008)
108. Tankanag A V, Chemeris N K *Biophysics* **54** 375 (2009); *Biofizika* **54** 537 (2009)
109. Mizeva I et al. *J. Biomed. Opt.* **20** 037007 (2015)
110. Frick P, Mizeva I, Podtaev S *Biomed. Signal Process. Control* **21** 1 (2015)
111. Martini R, Bagno A *Clin. Hemorheol. Microcirc.* **70** 213 (2018)
112. Dumler A A et al. *Al'manakh Klinicheskoi Meditsiny* **44** 179 (2016)
113. Stepanov R et al. *Biomed. Signal Process. Control* **36** 50 (2017)